Final Report for Period: 08/2007 - 07/2008
Submitted on: 11/21/2008
Principal Investigator: Landman, Uzi .
Award ID: 0304009
Organization: GA Tech Res Corp - GIT
Submitted By:
Brand, Oliver - Co-Principal Investigator
Title:
NIRT: NANOJETS - Formation, Characterization and Applications

Project Participants

Senior Personnel

Name: Landman, Uzi
Worked for more than 160 Hours: Yes
Contribution to Project:

Name: Glezer, Ari
Worked for more than 160 Hours: Yes
Contribution to Project:

Name: Allen, Mark
Worked for more than 160 Hours: Yes
Contribution to Project:

Name: King, William
Worked for more than 160 Hours: Yes
Contribution to Project:

Name: Brand, Oliver
Worked for more than 160 Hours: Yes
Contribution to Project:

Name: Luedtke, William
Worked for more than 160 Hours: Yes
Contribution to Project:
Molecular dynamics simulations of nanojets injected into gaseous enviroment
Setting up computer code for molecular dynamics simulations of propane nanojets with embedded gold nanocrystallites

Name: Gao, Jianping
Worked for more than 160 Hours: Yes
Contribution to Project:

Post-doc

Graduate Student

Name: Naik, Nisarga
Worked for more than 160 Hours: Yes
Contribution to Project:
Fabrication of nanojet orifices

Name: Courcimault, Christophe

Worked for more than 160 Hours: Yes
Contribution to Project:
Fabrication of nanojet orifices

Name: Lee, Jay
Worked for more than 160 Hours: Yes
Contribution to Project:
Prototype nanojet printing system

Name: Wright, Tanya
Worked for more than 160 Hours: Yes
Contribution to Project:
Fabrication of AFM cantilevers for nanojet metrology

Name: Berg, John
Worked for more than 160 Hours: Yes
Contribution to Project:
Fluidic system and optical diagnostics for micro- and nanoscale jets

Name: Tandon, Prateek
Worked for more than 160 Hours: Yes
Contribution to Project:
Design of resonant cantilever sensors for nanojet metrology

Name: Schweizer, Thomas
Worked for more than 160 Hours: Yes
Contribution to Project:
Investigation of piezoresistivity in polymers for nanojet metrology

Name: Kang, Wei
Worked for more than 160 Hours: Yes
Contribution to Project:
Molecular dynamics simulations of nanojets injected into gaseous enviroment

Name: Naeli, Kianoush
Worked for more than 160 Hours: Yes
Contribution to Project:
Design, fabrication and test of microstructurres for nanojet metrology.

Undergraduate Student

Technician, Programmer

Other Participant

Research Experience for Undergraduates

Organizational Partners

Other Collaborators or Contacts

Activities and Findings

Research and Education Activities: (See PDF version submitted by PI at the end of the report)

Findings: (See PDF version submitted by PI at the end of the report)

Training and Development:

Work in this project contributed significantly to the training of nine graduate students and two post-doctoral fellows (senior research scientists).

Three graduate students were involved in the fabrication of the nanojet 'hardware', including the nm-scale orifices and the fluidic handling system, training them in various aspects of micro- and nanofabrication as well as microfluidics.

Five graduate students were involved in developing the metrology tools for the nanojet characterization, involving the design and fabrication of cantilever-based microsensors and the set-up of a testing platform. These students were trained as well in various aspects of micro- and nanofabrication and in microsystem metrology.

One graduate student and two postdocs were introduced to atomistic molecular dynamics simulations of nanojets, and they have achieved a level that allows them to perform independent work on this subject. Along with algorithmic issues, both individuals obtained training on the performance of nanojet simulations on parallel computers.

Of the nine graduate students, four have graduated with a PhD degree and three with an MS degree. Two additional PhD students are in the final stages of their research and are expected to graduate in 2009. In addition, several undergraduate students have participated in various aspects of the research (see Outreach Activities).

Outreach Activities:

Courses:

Prof. Landman taught at Georgia Tech a course (2004, 2005, 2006, 2007) on 'Physics of Small Systems', listed for both undergraduate and graduate students, and open to students from Georgia Tech as well as to students from Clark Atlanta University. The physics of nanojets and nanobridges constituted one of the chapters in this course.

K-12 Outreach:

Prof. Landman lectured in July 2007 in an International School for Young Scientists on Nanomaterials, in Tsukuba, Japan, organized jointly by the US NSF (through UCSB) and the Japanese Institute for Materials Science (Tsukuba). The School was attended by young scientists from 14 countries, including the USA, Africa, Japan, and Asia.

As part of the NNIN sponsored outreach activities targeting middle school students, Prof. Brand participated in a 'Ask a Scientist' session targeting nanotechnology.

Graduate Student Nisarga Naik acted as a mentor to a group of ten school children at the '2007 Centennial Place Nanoinfusion'. This outreach program targets on getting school children of various age groups acquainted with nanotechnology by lab tours and activities related to nanotechnology.

As part of the NNIN sponsored first NanoInfusion Days at Georgia Tech, graduate student Nisarga Naik presented her nanojet research activities to 8th grade students from Austin Road Middle School in Henry County, GA.

Prof. Landman gave presentations on æThe Physics of Small ThingsÆ to senior students at two Atlanta high schools.

Seminars:

Graduate student Nisarga Naik presented æNanojets -Fabrication and CharacterizationÆ at æNanotechnology ExplorationsÆ in 2004 at the Georgia Institute of Technology

Prof. Brand gave introductory lectures on Micro- and Nano Electro Mechanical Systems to minority undergraduate students during the 2005 and 2006 Georgia Tech Summer Undergraduate Research in Engineering (SURE) program at Georgia Tech.

At a Georgia Tech event to encourage female students to stay in electrical engineering and become engaged in research, Prof. Mark Allen gave a presentation on the micro- and nanotechnology activities in his research group.

Student Supervision:

As part of the 10-week Georgia Tech Summer Undergraduate Research in Engineering (SURE) program, Ariel Brown and Trista D. Martin, two minority students, performed research in Prof. BrandÆs laboratory.

Journal Publications

W. Kang, W.D. Luedtke, U. Landman, "Molecular Dynamics Simulations of Two-Phase Nanojets and Nanobridges", Bulletin of the American Physical Society, p. 443, vol. 50, (2005). Published,

W. Kang, U. Landman, "Breakup and Universality Regimes of Liquid Nano Structures: Molecular Dynamics and Stochastic Hydrodynamics", Physical Review E, p. , vol. , (2007). Submitted,

Kang, W; Landman, U, "Universality crossover of the pinch-off shape profiles of collapsing liquid nanobridges in vacuum and gaseous environments", PHYSICAL REVIEW LETTERS, p. , vol. 98, (2007). Published, 10.1103/PhysRevLett.98.06450

Kang, W; Landman, U; Glezer, A, "Thermal bending of nanojets: Molecular dynamics simulations of an asymmetrically heated nozzle", APPLIED PHYSICS LETTERS, p. , vol. 93, (2008). Published, 10.1063/1.298828

Lee, J; Hunter, H; Glezer, A; King, WP, "Phase change and cooling characteristics of microjets measured using microcantilever heaters", SENSORS AND ACTUATORS A-PHYSICAL, p. 64, vol. 147, (2008). Published, 10.1016/j.sna.2008.03.02

Lee, J; Hunter, H; Goericke, F; Naik, N; Allen, M; Glezer, A; King, WP, "Measurements of microjet cooling and phase change characteristics using microcantilever heaters", IPACK 2007: PROCEEDINGS OF THE ASME INTERPACK CONFERENCE 2007, VOL 1, p. 163, vol. , (2007). Published,

Lee, J; Naeli, K; Hunter, H; Berg, J; Wright, T; Courcimault, C; Naik, N; Allen, M; Brand, O; Glezer, A; King, W, "Micro-cantilever based metrology tool for flow characterization of liquid and gaseous micro/nanojets", Micro-Electro-Mechanical Systems - 2005, p. 95, vol. 7, (2005). Published,

Naik, N; Courcimault, C; Hunter, H; Berg, J; Lee, J; Naeli, K; Wright, T; Allen, M; Brand, O; Glezer, A; King, B, "Fabrication and characterization of liquid and gaseous micro-and nanojets", Micro-Electro-Mechanical Systems - 2005, p. 731, vol. 7, (2005). Published,

Naik, N; Courcimault, C; Hunter, H; Berg, J; Lee, J; Naeli, K; Wright, T; Allen, M; Brand, O; Glezer, A; King, W, "Microfluidics for generation and characterization of liquid and gaseous micro- and nanojets", SENSORS AND ACTUATORS A-PHYSICAL, p. 119, vol. 134, (2007). Published, 10.1016/j.sna.2006.04.05

Lee, J; Naeli, K; Hunter, H; Berg, J; Wright, T; Courcimault, C; Naik, N; Allen, M; Brand, O; Glezer, A; King, WP, "Characterization of liquid and gaseous micro- and nanojets using microcantilever sensors", SENSORS AND ACTUATORS A-PHYSICAL, p. 128, vol. 134, (2007). Published, 10.1016/j.sna.2006.05.01

Naeli, K; Brand, O, "Coupling high force sensitivity and high stiffness in piezoresistive cantilevers with embedded Si-nanowires", 2007 IEEE SENSORS, VOLS 1-3, p. 1065, vol. , (2007). Published,

Naeli, K; Tandon, P; Brand, O, "Geometrical optimization of resonant cantilever sensors", TRANSDUCERS '07 & EUROSENSORS XXI, DIGEST OF TECHNICAL PAPERS, VOLS 1 AND 2, p. U126, vol. , (2007). Published,

Naeli, K; Brand, O, "Cantilever sensor with stress-concentrating piezoresistor design", 2005 IEEE Sensors, Vols 1 and 2, p. 592, vol. , (2005). Published,

Landman, U, "Materials by numbers: Computations as tools of discovery", PROCEEDINGS OF THE NATIONAL ACADEMY OF SCIENCES OF THE UNITED STATES OF AMERICA, p. 6671, vol. 102, (2005). Published, 10.1073/pnas.040803810

Chui, BW; Aeschimann, L; Akiyama, T; Staufer, U; de Rooij, NF; Lee, J; Goericke, F; King, WP; Vettiger, P, "Advanced temperature compensation for piezoresistive sensors based on crystallographic orientation", REVIEW OF SCIENTIFIC INSTRUMENTS, p. , vol. 78, (2007). Published, 10.1063/1.272238

Lee, J; King, WP, "Microcantilever hotplates: Design, fabrication, and characterization", SENSORS AND ACTUATORS A-PHYSICAL, p. 291, vol. 136, (2007). Published, 10.1016/j.sna.2006.10.05

Nelson, BA; King, WP, "Temperature calibration of heated silicon atomic force microscope cantilevers", SENSORS AND ACTUATORS A-PHYSICAL, p. 51, vol. 140, (2007). Published, 10.1016/j.sna.2007.06.00

N. Naik, M. Allen, "Fabrication of glass-metal composite micro/nanonozzles", Proc. ASME IMECE 2008 Conference, p. , vol. , (2008). Accepted,

O. Brand, K. Naeli, S. Demirci, S. Truax, J.H. Seo, "Silicon-Based Resonant Microsensors", Proc. Micromechanics Europe Workshop, p. , vol. , (2008). Published,

K. Naeli, O. Brand, "Cancellation of environmental effects in resonant mass sensors based on overtones and effective mass", Review of Scientific Instruments, p. , vol. , (2008). Submitted,

K. Naeli, O. Brand, "Dimensional considerations in achieving large quality factors for resonant silicon cantilevers in air", Journal of Applied Physics, p. , vol. , (2008). Submitted,

Books or Other One-time Publications

Web/Internet Site

Other Specific Products

Contributions

Contributions within Discipline:

The project ôNIRT: Nanojets: Formation, Characterization and Applicationsö has contributed significantly to the knowledge, theory and research methods in the areas of fluid dynamics, in particular the understanding of micro- and nano-scale liquid jets, and of microsystems technology, e.g. the application of cantilever probes capable for operation in harsh environment for in-situ diagnostics of these jets. The experimental work on microjets enabled fundamental studies of the influence of jet column instabilities on the flow characteristics with specific emphasis on atomization. In the area of microsystems technology, the nanojet project has resulted in manufacturing processes that enable the batch fabrication of sub-micrometer nozzles, which can withstand system pressures exceeding 100 bar. Moreover, heated and piezoresistive cantilever platforms enabling a wide range physical and chemical measurements with micrometer or even sub-micrometer resolution have been devised. The work with liquid micro- and nanojets resulted in the development of measurement techniques that are applicable to harsh environments over a broad range of ambient pressures and with rapidly changing temperatures.

Contributions to Other Disciplines:

The findings of the NIRT project are widely applicable to other disciplines. A better understanding of the influence of instabilities on the characteristics of micro- and nano-scale liquid jets will potentially allow to optimize such jets in a broad range of applications including inkjet printing, micro- and optoelectronics device fabrication, and future applications that include drug delivery and direct printing of nanometer-scale patterns. The developed knowledge of cantilever probes will also have a broad range of applications, such as materials characterization or bio(chemical) sensing. As an example, a compensation technique developed during the nanojet project to make mass-sensitive cantilever sensors less susceptible to temperature and humidity changes is currently applied to reduce the long-term drift in chemical microsensors and, thus, improve their resolution in environmental monitoring (e.g. O. Brand, K. Naeli, K.S. Demirci, S. Duerson, J.H. Seo, Proc. Micromechanics Europe Workshop 2008). Moreover, the heated cantilevers developed to investigate micro- and nanojet flow characteristics can be applied to e.g. nanometer-scale surface patterning (e.g., Y. Hua, W.P. King, C.L. Henderson, Microelectronics Engineering 85 (2008) 934-936) or microthermogravimetry (e.g., J. Lee, W.P. King, Review of Scientific Instruments 79 (2008) 54901).

Contributions to Human Resource Development:

Nine graduate students and two post-docs have been trained as part of the NIRT project in a highly interdisciplinary environment involving physicists, electrical engineers and mechanical engineers. By the end of 2008, four PhD and 3 MS students have ôgraduatedö from the project; two additional PhD students will graduate in 2009. In addition, several undergraduate engineering students participated in the research as part of their ôundergraduate research experienceö.

Contributions to Resources for Research and Education:

Contributions Beyond Science and Engineering:

It is anticipated that the technologies that were developed under the NIRT program for the realization of of micro- and nano-scale liquid jets, and of the microsystems technologies associated with cantilever probes for in-situ diagnostics in harsh environment will have significant commercial potential. Applications will include various microscale pattern printing technologies for the fabrication of microelectronic hardware and for precision medical drug delivery. The developed technology of cantilever probes can be used for materials characterization and bio-chemical sensing.

Categories for which nothing is reported:

Organizational Partners

Any Book
Any Web/Internet Site
Any Product
Contributions: To Any Resources for Research and Education

NIRT: Nanojets – Formation, Characterization and Applications

Final Report 2008: Project Findings

U. Landman (PI), School of Physics
M.G. Allen, O. Brand, School of Electrical and Computer Engineering
A. Glezer, School of Mechanical Engineering

Georgia Institute of Technology, Atlanta, GA 30332

W.P. King, Mechanical Science and Engineering

University of Illinois at Urbana-Champaign, Urbana, IL 61801

Orifice Fabrication

- Developed new fabrication technologies for in-plane silicon micro/nanonozzles (dimension range: 500 nm to 12 μm) and circular glass-metal composite micro/nanonozzles (dimension range: 430 nm to 100 μm).
- Demonstrated high pressure (>10 MPa) withstanding capacity of the microfabricated nozzles.
- Demonstrated feasibility of generating pressure-driven fluidic nanojets using the microfabricated nanonozzles.

Optical Characterization of Micro/Nanojets

- A range of instabilities of evaporating microscale jets (including column modes, bifurcations, and atomization) have been identified and characterized over a range of operating parameters. The appearance of vapor bubbles within the jet column has a profound effect on the jet structure and can lead to very intricate breakup and branching.
- Varicose and sinuous instability modes were identified in micro-scale jets. It is shown that when the varicose instability mode dominates, jet breakup distance increases with Reynolds number. However, when the sinuous instability dominates the break up distance decreases with increasing Reynolds number.
- The appearance of vapor bubbles within the jet column has a profound effect on the jet structure and can lead to very intricate breakup and branching.

Cantilever-Based Metrology Tools for Micro/Nanojet Characterization

- Developed and fabricated heated and piezoresistive cantilever sensors for static and dynamic interrogation of micro- and nanojets; thereby, the investigated microsensors have applications beyond micro- and nanojet metrology in areas ranging from force sensing to chemical sensing.
- Developed compensation techniques for environmental parameters (e.g. temperature, humidity, and pressure) for cantilever-based microsensors; again, the developed techniques are applicable in harsh environment applications beyond micro- and nanojet metrology.
- Optimized the force sensitivity of piezoresistive cantilevers using stress-concentration principles without sacrificing the stiffness of the cantilever, yielding robust yet highly sensitive cantilever designs for harsh-environment testing.
- The thermal interaction of liquid microjets with heated surfaces can be effectively investigated using heated cantilevers as metrology tool. Operation conditions could be identified where the cooling of the heated surface by the microjet is most effective.
- A method to determine the breakup distance for microjets based on piezoresistive cantilevers was developed.

Molecular Dynamics Simulation of Nanojets

- Developed new concept for generating sub-μm jets based on a heated nozzle, termed virtual nanojet nozzle and verified its feasibility by molecular dynamics simulations and a continuum hydrodynamics model. The goal is to generate nanometer-scale jets from larger diameter orifices, thus simplifying the fabrication process and the reducing the pressure requirements for the jet generation.
- Liquid propane nanojets and nanobridges were found through molecular dynamics simulations to exhibit in vacuum a symmetric break-up profile shaped as two cones joined in their apexes. This mode of breakup results in a sharply peaked drop size distribution. With a surrounding gas of sufficiently high pressure, a long-thread profile develops with an asymmetric shape. The emergence of a long-thread profile, discussed previously for macroscopic fluid structures, originates from the curvature-dependent evaporation-condensation processes of the liquid nanostructure in a surrounding gas. A modified stochastic hydrodynamic description captures the crossover between these universal break-up regimes.

NIRT: Nanojets – Formation, Characterization and Applications

Final Report 2008: Project Activities

U. Landman (PI), School of Physics
M.G. Allen, O. Brand, School of Electrical and Computer Engineering
A. Glezer, School of Mechanical Engineering

Georgia Institute of Technology, Atlanta, GA 30332

W.P. King, Mechanical Science and Engineering

University of Illinois at Urbana-Champaign, Urbana, IL 61801

0. Introduction

The following report summarizes the research activities carried out under the NIRT program "Nanojets – Formation, Characterization and Applications" between 2003 and 2008. The research activities are sub-divided into the nanojet orifice fabrication (Chapter I), the development of the nanojet fluidic system and the optical characterization of micro- and nanojets (Chapter II), the development and testing of cantilever-based metrology tools for nanojet characterization (Chapter III), and the nanojet simulation efforts (Chapter IV).

I. Nanojet Orifice Fabrication

I.1 Overview

This part of the project focuses on the fabrication of micro/nanonozzles capable of generating stable liquid and gaseous micro/nanojets. Two different approaches have been used to fabricate the nozzles. The first approach utilizes conventional microfabrication techniques such as lithography, wet etching, and fusion bonding, to build in-plane silicon micro/nanonozzles with orifice dimensions ranging from 500 nm to 12 μm. The second method involves mechanical reinforcement of pulled glass micropipettes using nickel electroplating to fabricate nozzles with orifice diameters ranging from 430 nm to 100 μm. These nozzles are then integrated with a high-pressure fluidic setup to drive and investigate liquid and gaseous micro/nanojets.

I.2 In-Plane Silicon Nozzles

This section reports the fabrication of in-plane silicon micro/nanonozzles with dimensions ranging from 500 nm to 12 μm. The silicon micro/nanonozzles were designed to sustain high-pressure drops necessary to obtain substantial micro/nanofluidic jet flows. The dimensions of the channel, and the fluidic reservoir were defined by design and not by fabrication constraints.

Fig. I.1 depicts the fabrication sequence of the nozzles. Silicon dioxide was grown (Fig.I.1a) on a double-side polished 450 µm thick (100) silicon wafer. Standard photolithography was performed to delineate the nozzle structure (Fig.I.1b). Anisotropic potassium hydroxide (KOH) etching (concentration of KOH = 40% at 70˚C) was carried out to etch channels and reservoirs into the silicon substrate (Fig.I.1c). After etching away silicon dioxide, the wafer was fusion bonded with another silicon wafer, and annealed at 1100 ˚C for 4 hours, forming enclosed nozzles (Fig.I.1d). The nozzles were then individualized using a through-wafer Inductively Coupled Plasma (ICP) etch or alternatively by dicing (Fig.I.1e). The top surface of the nozzles containing the orifice outlet was polished using chemical mechanical polishing (Fig.I.2). This removed any fabrication imperfection on the exit plane. Oxidative sealing was then optionally utilized to reduce the inner dimensions of the nozzles to submicron range (Fig.I.1f).

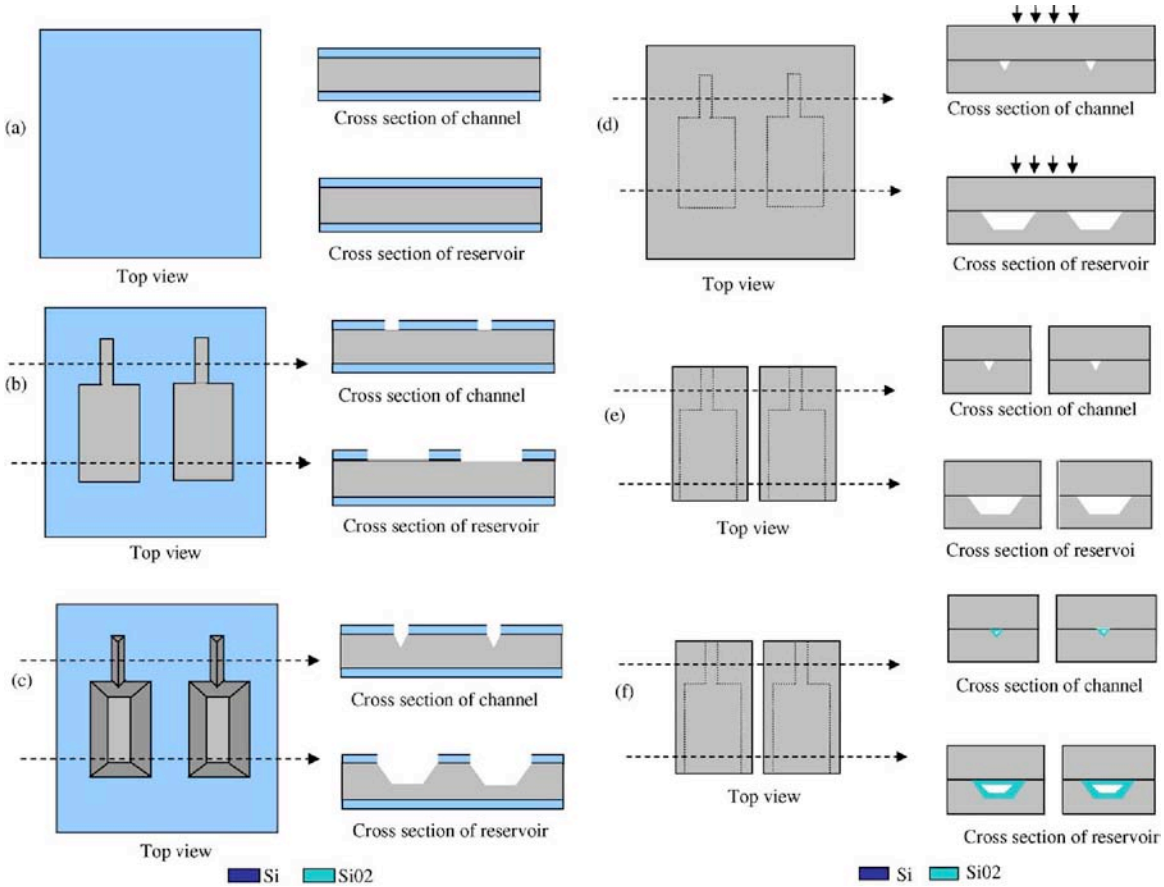

Figure I.1: *Fabrication sequence, a) silicon dioxide is deposited on both sides of the wafer, b) silicon dioxide is patterned, c) anisotropic wet etching is performed to etch the channel and the reservoir, d) silicon to silicon fusion bonding is performed to enclose the nozzles, e) dies are separated by through wafer silicon etch by ICP or dicing and f) the nozzles are optionally oxidized to reduce the orifice dimension from micrometer to nanometer scale.*

Length and width of the channel, and width and depth of the reservoir were alterable by design (Fig.I.3a). The dimensions of the reservoir were optimized in order to minimize the interior surface area of the reservoir, while obtaining a maximum possible entry (cross section) surface area for the fluid. This optimization was an effort to reduce the

reservoir surface area facing the fluid pressure, increasing the pressure withstanding capacity of the nozzle. The channel length was chosen to be ten times the channel width in order to ensure the generation of a fully developed flow. KOH etching was employed to define a triangular channel with very a small cross section area, while etching a deeper reservoir (Fig.I.3). With a timed etch, the required depth of the reservoir was obtained while the depth of the channel was dictated by the channel width and anisotropic etch stop due to intersection of the slowest etching (111) planes [1]. These planes of the nozzle channel were believed to offer smooth walls for fluid flow. Also the undercut of the convex corners, and the ramp between the reservoir and the channel were believed to offer a gradual transition for the fluid from the reservoir to the channel. For concentration of KOH= 40% at 70 ◦C, the undercut of convex corners (in *x* and *y* directions) was roughly 2.5-times the etch rate of the depth (*z* direction).

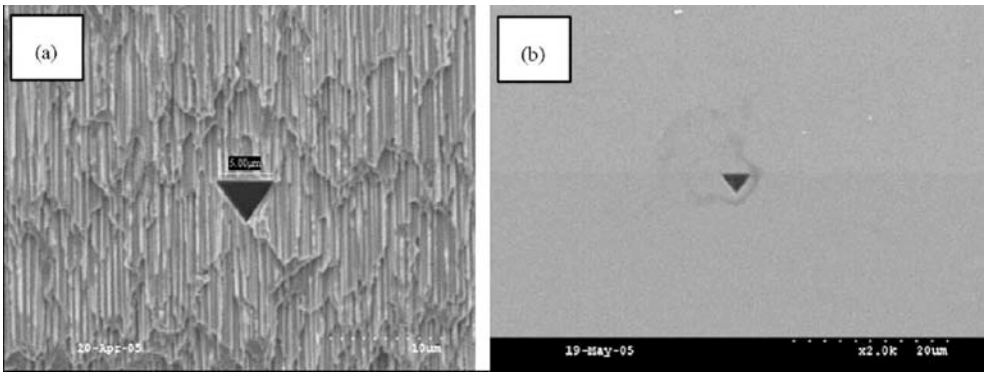

Figure I.2: *The exit plane of the nozzle, a) showing the surface roughness after an ICP etch is performed to separate the dies and b) after performing Chemical Mechanical Polishing (CMP) to smoothen out any fabrication imperfection.*

Further thermal oxidation of the individualized nozzles was employed for scaling down the orifice sizes from micron to submicron range. Fig.I.4 shows a 500 nm nozzle obtained after a 16 hours long wet oxidation at 1100 °C of a 3 μm triangular nozzle. Nanoscale orifices were obtained without resorting to serial processing nanofabrication techniques.
Variations of the above design were obtained by an additional mask step. To obtain a rectangular cross section orifice, the reservoir was etched by KOH etching in order to obtain the gradual ramp; while the nozzle channel was etched by ICP etching (Fig.I.5a). A near-circular cross-section channel was obtained by oxidizing the triangular channel and etching the grown silicon dioxide with hydrofluoric acid. The oxidation rate towards the corners of the triangles was smaller compared to that along the rest of the edge, leading to a nonuniform oxide profile along the edge (Fig.I.5c). Thus, the corners were rounded off when the oxide was etched away.

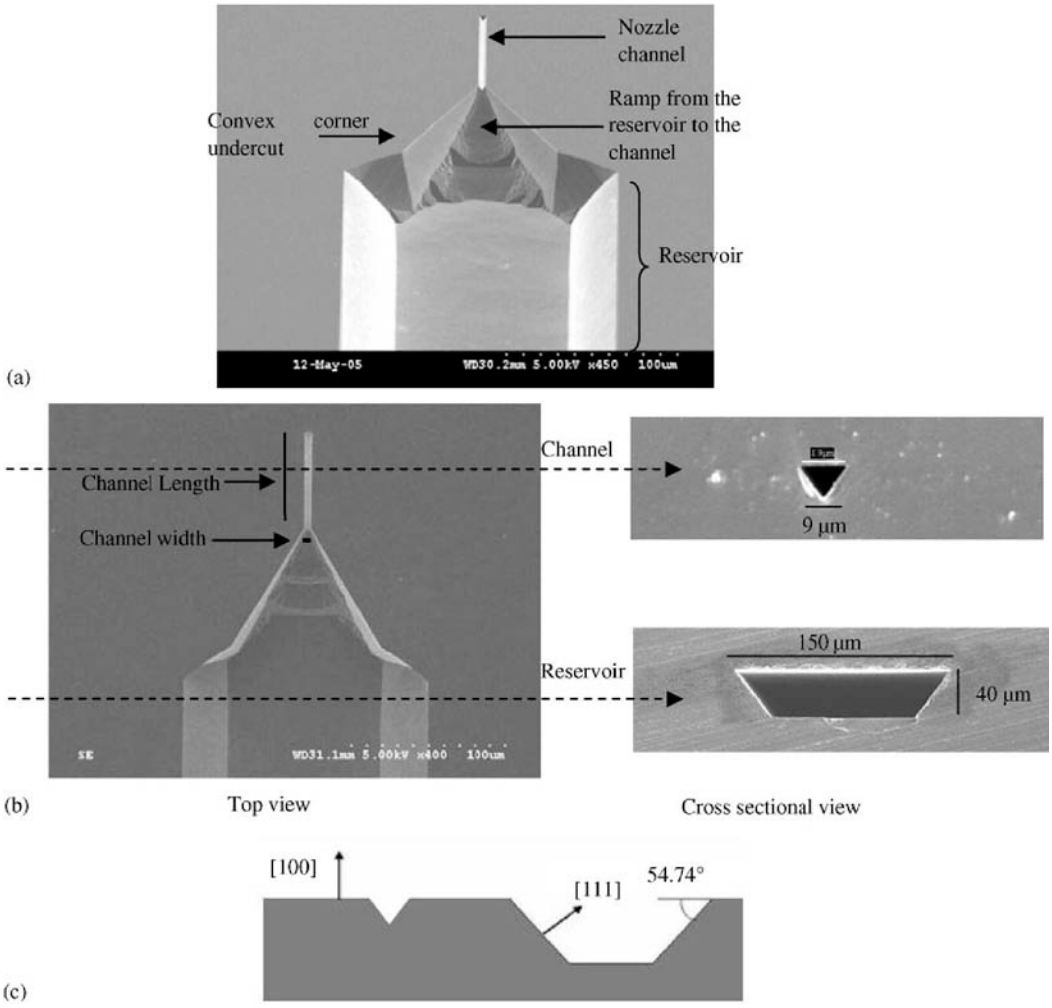

Figure I.3: *SEM images of KOH etched nozzle, a) tilted view showing different parts of the nozzle namely the channel, the reservoir and the ramp, b) top view and cross sectional view and c) schematic of KOH etch profile.*

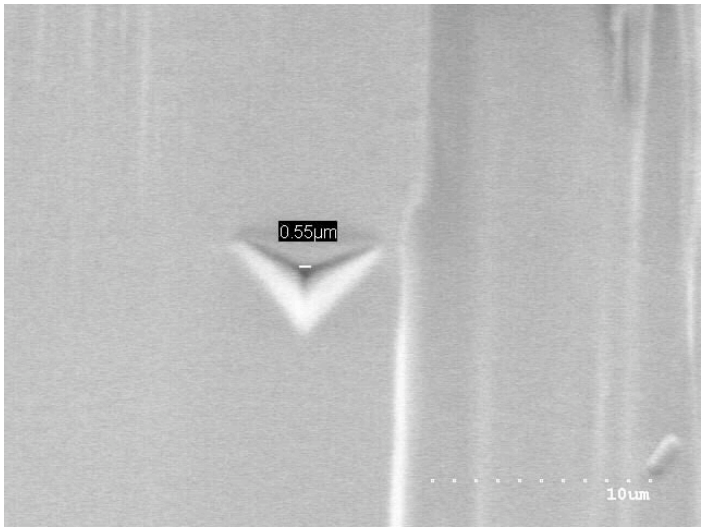

Figure I.4: *SEM image of a 500 nm nozzle obtained by the thermal oxidation of a 3 µm silicon nozzle.*

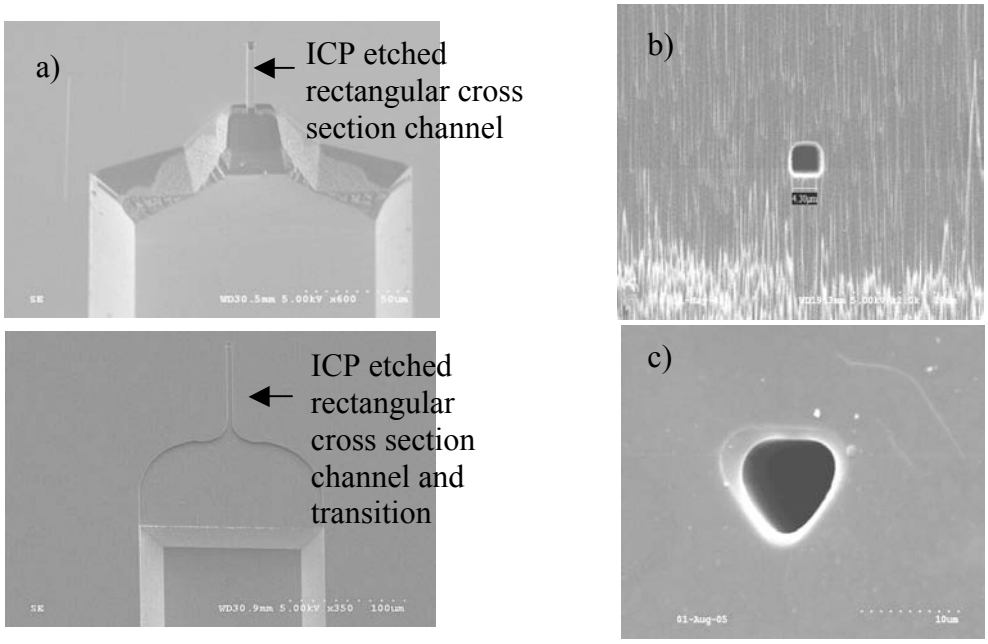

Figure I.5: *a) SEM images of different nozzle designs fabricated using an additional mask step to build the channel and reservoir in different steps; SEM images of cross section of b) a 4 µm by 4 µm rectangular cross section nozzle, c) a 9 µm rounded triangular cross section nozzle obtained after oxidation of a 7 µm nozzle and stripping the oxide.*

I.3 Nickel Plated Glass Nozzles

Unlike the conventional methods used to fabricate micro/nanonozzles, the fabrication technique discussed in this section is a non-lithographic approach. It uses pulled borosilicate micropipettes as a foundation and nickel as a strengthening layer to build high pressure withstanding micro/nanonozzles. Pipettes built using the pulling process are axis-symmetric and offer a smooth transition to the fluid from the reservoir to the tapered part of the nozzle, providing an ideal geometry from fluid flow and stress point of view. These nozzles can be easily interfaced with a macro high pressure fluidic setup to drive fluidic micro/nanojets. Also since the material of the nozzle is metallic, induction-based non-contact heating of the nozzle can be used in applications requiring temperature control [2].

The fabrication sequence of glass-metal composite nozzles is illustrated in Fig.I.6. Borosilicate glass capillaries were pulled into micro/nanopipettes using P-97 Micropipette puller, manufactured by Sutter Instrument Company (Fig.I.7a). By varying the machine parameters such as the heat supplied to the capillary, the velocity of the glass carriage under constant load at which the hard pull is applied, the force of the hard pull and the air cooling time, the tip diameter and the taper length of the micropipette were modified, hence providing control over the nozzle dimensions [3,4]. The glass micropipette was sputter coated with a Titanium/Copper (Ti/Cu) seed layer, followed by electroplating a 20-50 μm thick layer of nickel (Fig.I.7b). This step concealed the entire glass pipette including the micro/nano orifice tip. The metal reinforcement enabled the glass nozzles to withstand pressures upto 10.5 MPa (1500 psi). In order to uncover the concealed orifice, focused ion beam (FIB) milling was employed to precisely mill out the top layer of nickel from the nozzle tip (Fig.I.7c). Using this technique, nozzles with tip diameters ranging from 430 nm to 100 μm were fabricated. Fig.I.8 shows the SEM images of a 430 nm diameter nanonozzle and a 100 μm diameter micronozzle fabricated by this technique. The FIB milling step could be substituted with sandpaper polishing of the nozzle tip to grind away excess metal; though this did not provide an adequate control over the final orifice diameter. A purely nickel nozzle was built by etching away the glass support (Fig.I.9a). This technique was further applied to build metal multibarrel micropipettes (Fig.I.9b), coaxial micropipettes (Fig.I.9c) and multi orifice micropipettes (Fig.I.9d). Also micronozzles for applications requiring a confined heating of the nozzle such as localized tip heating rather than bulk heating, were fabricated by localized electroplating (Fig.I.10). This was achieved by selectively leaving the desired portion of the glass support uncoated with metal by concealing it while electroplating.

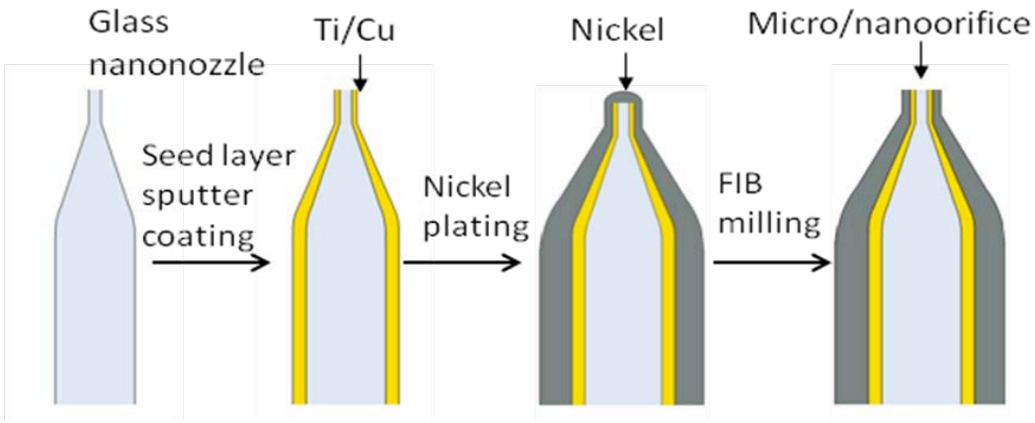

Figure I.6*: Fabrication sequence of glass-metal composite micro/nanonozzle.*

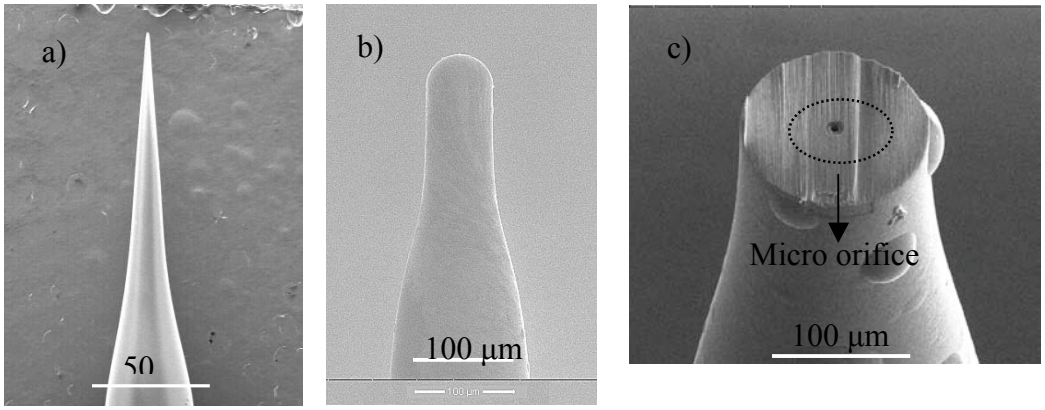

Figure I.7*: SEM images of, a) a glass micropipette pulled using the micropipette puller, b) a micronozzle after electroplating with nickel, c) a micronozzle after FIB milling to reveal the micro orifice tip.*

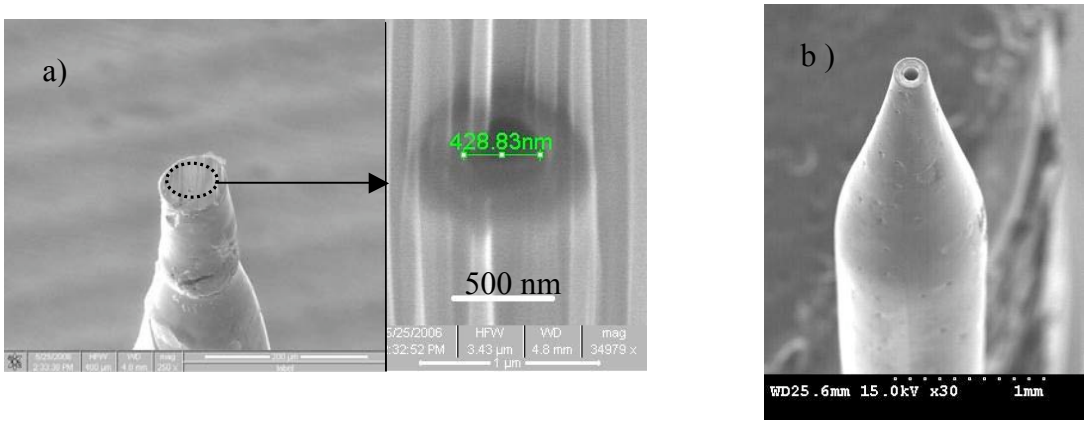

Figure I.8*: SEM image of, a) a 430 nm glass-metal orifice, b) a 100 µm glass-metal nozzle.*

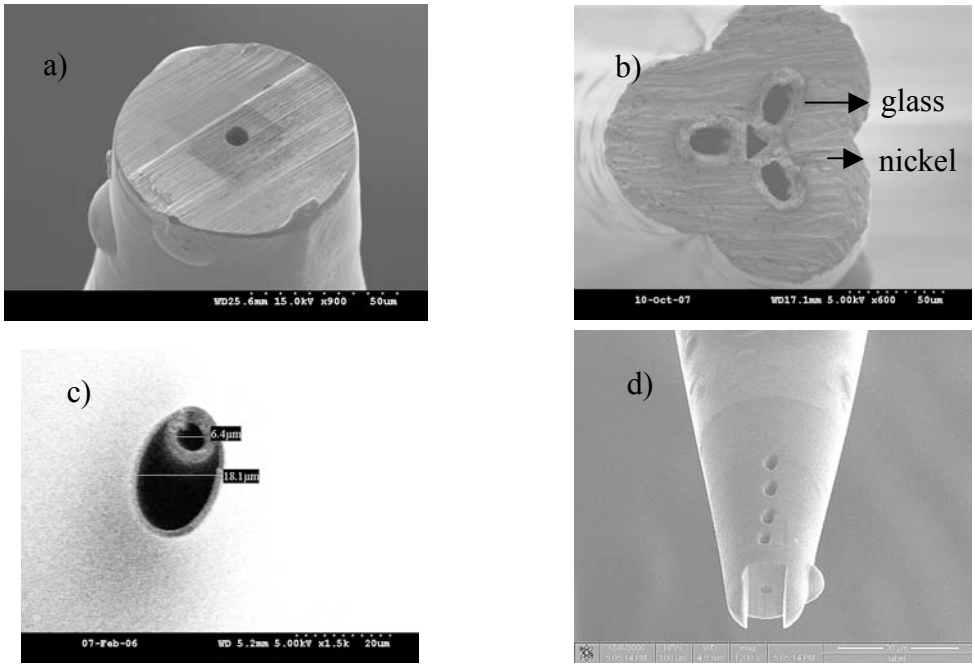

Figure I.9*: SEM images of, a) a nickel micronozzle of 8 μm diameter with the glass layer etched out, b) top view of a 3-barrel glass-nickel micronozzle, c) coaxial micronozzles, d) a metal micronozzle with 5 orifice exits.*

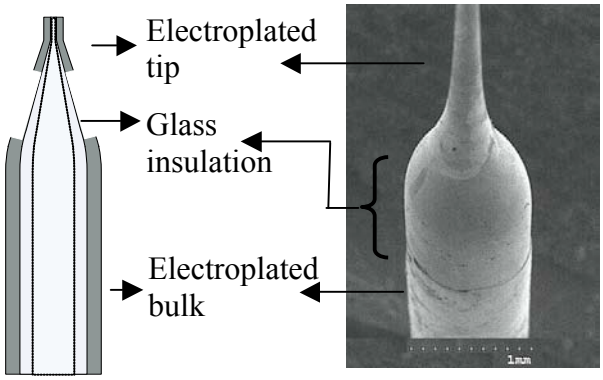

Figure I.10*: a) Schematic of a partially electroplated nozzle for localized tip heating, b) SEM image of a partially electroplated nozzle.*

I.4 Packaging

The microfabricated nozzles were integrated with the pressure generation apparatus using a machined stainless steel plate acting as a micro-to-macro interface (Fig.I.11). An epoxy was used to mount the nozzles to form a leak proof interface with the fluid setup. A laser shadowgraphy technique was used to visualize and image the jet flows. Micromachined heated and piezoresistive cantilevers were used to investigate the thrust and heat flux

characteristics of the jets. Testing of the nozzles and characterization of the jets are discussed in the following sections.

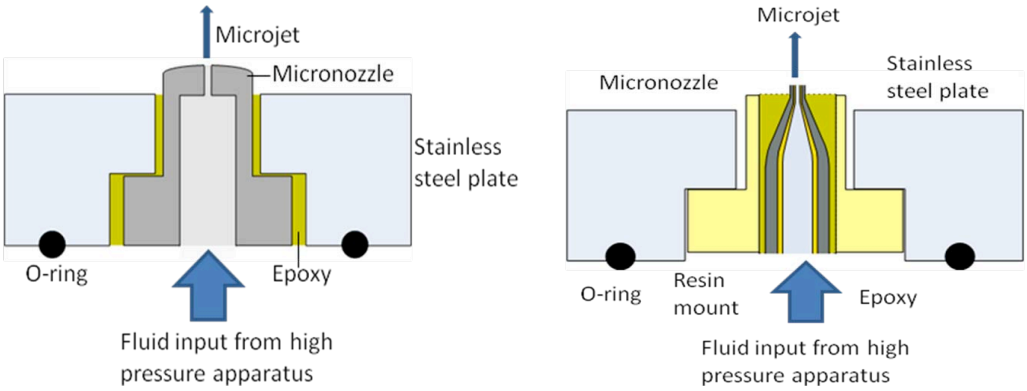

Figure I.11: *Schematic of stainless steel/resin macro to micro interface for a) silicon nozzles, b) glass-metal composite nozzles*

I.5 Induction Heating of Glass-Nickel Nozzles

The nickel coating on the glass nozzles not only increased the mechanical strength of the nozzles, but also enabled heating of the liquid jets in flow. Fig.I.12 indicates the schematic of a noncontact-based induction heating setup for the nozzles. The goal of heating the microjets was to prevent clogging and jet deterioration due to ice formation and investigate the effect of heat on the jet flow.

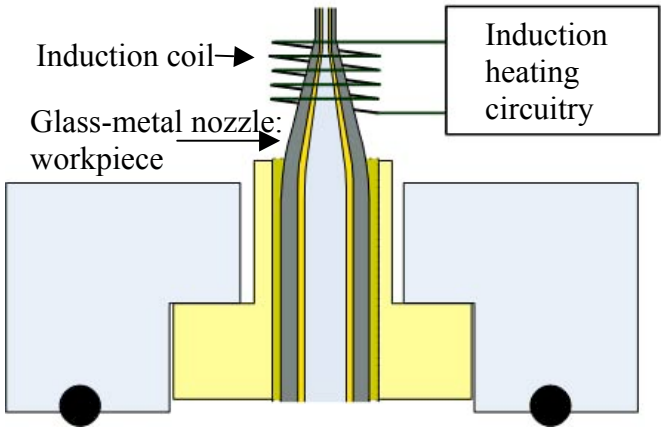

Figure I.12: *Cross-sectional schematic of the setup for induction heating of nickel nozzle.*

The induction heating apparatus consisted of:

1) A glass-nickel micronozzle (tip inner diameter ranging from 5 µm to 20 µm) acting as the workpiece.
2) Induction heating circuitry
3) High pressure fluidic setup to drive liquid microjets
4) Stainless steel and epoxy mount to interface the nozzle with the fluidic setup

The induction heating circuitry consisted of an H-bridge (IC LM18200T from National Semiconductor) and a resonant LC circuit with the heating coil. The heating setup was designed to drive at a frequency of 109 KHz heating a skin depth of 15-25 μm of the metal layer of the nozzle.
The heating system was:

- Capable of heating the bulk and the tip of the nozzle
- Capable of measuring the temperature of the nozzle bulk using a very fine thermocouple and a thermocouple meter
- Capable of controlling the equilibrium temperature by varying the duty cycle for the power supplied to the coil

Experiments were performed with no heating, various duty cycles (20%, 50%, 80%) and no modulation heat control i.e. full power. This gave different equilibrium temperatures.
With the heating turned, the following was observed:

- The breakup distance of the jets decreased
- There wasn't a significant change in the velocity

With different duty cycles, the breakup distance fluctuated in accordance with the modulation

I.6 Nanojet Generation

The feasibility of driving nanojets using microfabricated nanonozzles was demonstrated. A propane jet spray was obtained from a 500 nm in-plane silicon nozzle at 12MPa (1750 psi). The jet was imaged using an overhead CCD camera (Fig.I.13a). Also a 900 nm propane jet was generated using a glass-metal composite nanonozzle at 7 MPa (1000 psi) (Fig.I.13b).

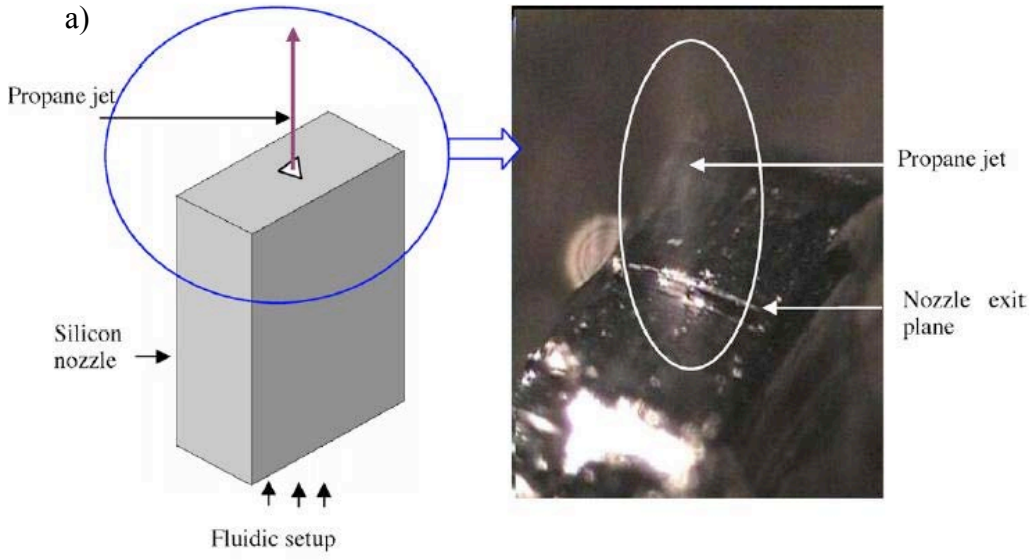

b)

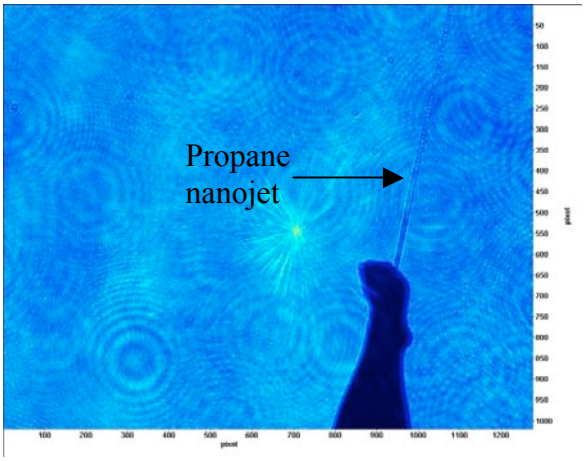

Figure I.13: *a) CCD camera image of a propane jet spray driven through a 500 nm silicon nozzle, b) shadowgraph of a 900 nm propane jet driven through a glass-metal nanonozzle*

I.7 Conclusion

Fabrication techniques for in-plane silicon micro/nanonozzles and glass-metal micro/nanonozzles have been developed. These fabrication techniques offer design flexibility and a high pressure withstanding capacity. Scalability and ease of integration with a macro pressure generation apparatus have been demonstrated for these nozzles. Also, noncontact heating of the nozzles has been demonstrated with the glass-metal nozzles.

References

1. Shikida, M., Sato, K., Tokoro, K., and Uchikawa, D., 2000, "Differences in anisotropic etching properties of KOH and TMAH solutions", *Sensors and Actuators A (Physical)*, A80(2), pp 179-88.
2. Park, J.-W., Park, J.-H., Yoon, Y.-K., Joung, Y.-H., Choi, S.-O., Prausnitz, M.R., Allen, M.G., 2005, "Wireless thermal micro-ablation of skin for transdermal drug delivery", *TRANSDUCERS '05. The 13th International Conference on Solid-State Sensors, Actuators and Microsystems. Digest of Technical Papers* (IEEE Cat. No. 05TH8791), pp 1238-1241.
3. Purves, R.D., 1980, "The mechanics of pulling a glass micropipette", *Biophysical Journal*, 29(3), pp 523-529
4. P-97 Micropipette puller manual, Sutter Instrument Company (www.sutter.com)

II. The Evolution of Micro-Scale Jets

II.1 Overview

The fluidic component of the NIRT Project focused on investigation of the fundamental flow mechanisms of micron-scale free liquid jets and characterization of their evolution. Specifically, the present work has investigated the break up of the liquid jet column, which is the result of the onset and amplification of several distinct instability modes including Rayleigh instability, sinuous instability, sinuous instability with atomization, evaporative instability, and flashing instability. The Rayleigh instability is driven by surface tension and the breakdown of the jet column at the most amplified streamwise wavelength results in the formation regularly spaced droplets. Sinuous instability occurs when the jet column begins to undulate and ultimately breaks down to a train of droplets. Sinuous instability with atomization is characterized by an undulated jet column that sheds fine droplets having characteristic diameters on the order of 0.1D. Evaporative instability is associated with asymmetric surface tension that is caused by asymmetric evaporation across the jet column. These asymmetries lead to column bending, the development of vapor pockets, and branching into multiple jet columns. Flashing instability is characterized by the appearance of vapor bubbles within the jet column that rupture and disrupt the jet column. The jet can develop either a segmented column or breakdown to atomized spray, depending on the rate of vapor bubble formation. The present work was conducted using jet nozzles fabricated by laser drilling in thin stainless steel membranes and then coated with an oleophobic monolayer to fix surface wetting properties. Diagnostics were based on optical imaging with field of view as small as [O(100μm)].

II.2 Experimental Apparatus

The set up of the present system is shown schematically in Fig. II.1. The test liquids are propane, butane, hexane, and octane which have similar chemical properties, but different physical properties, such as surface tension and vapor pressure (shown in Table III.1). The maximum operating pressure of the present system is 12.8MPa (2,000psi). In this system, nitrogen is used for pressurization. The system is filled with the working fluid and then pressurized using nitrogen (above the liquid level) to the desired working pressure. The jet nozzle is directly connected to the reservoir and is designed to minimize volume and the possibility of nitrogen pockets. The nozzle assembly is mounted on a 4 axis traverse system that includes translation in x, y, z, a rotational stage, and a goniometric platform for tilting the nozzle relative to the plane of the CCD array in the imaging camera. The pressure in the nozzle assembly is monitored using a pressure transducer. During Year IV, the nozzles used were fabricated from laser drilled stainless steel and coated with a oleophobic monolayer (which prevents nozzle fouling from hydrocarbon jets). Each nozzle is mounted on a steel flange that is designed to be attached to the reservoir. The nozzles are interchangeable.

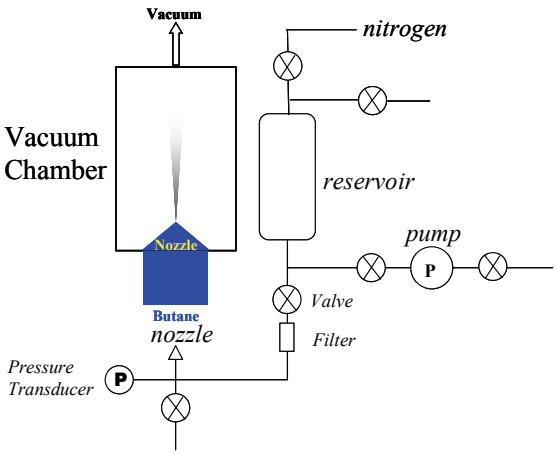

Figure II.1: *Fluidic system diagram*

The jet flow is visualized using shadowgraph imaging (the optical setup is shown in Fig. II.2). The flow field is illuminated using a (double-pulse) ND:Yag laser (532 nm) where the duration of the laser pulse is on the order of 5 ns. Instantaneous images of the flow are captured using a PIV CCD camera having 1008 x 1018 pixels and equipped with a high-magnification microscope lens. The lens system consists of both 5X and 50X infinity corrected microscope objective lenses coupled with a 6.5X lens and a 2X extension tube for a total maximum magnification of 228X. The smallest field of view is 28 μm on a side (i.e., approximately 28 nm per pixel).

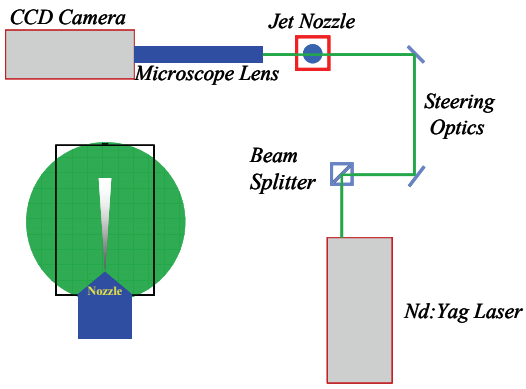

Figure II.2: *The shadowgraph imaging system*

	Density (kg/m^3)	Absolute Viscosity (mPa*s)	Surface Tension (mN/m)	Boiling Point (Celsius)	Vapor Pressure (kPa)	Ohnesorge d=10 μm
Hexane	655	0.296	17.9	69	20.00	0.027
Butane	575	0.158	11.8	-0.5	243.39	0.019
Propane	492	0.097	7	-42.1	951.51	0.017
Octane	698	0.509	21.2	125.5	1.85	0.042

Table III.1 *Test liquid properties. All properties are evaluated at 25 ºC except those liquids whose boiling points are below 25 ºC, in which case properties are determined at boiling point. Vapor pressure is determined at nominal temperature regardless of boiling point.*

II.3 Investigation of Jet Column Instabilities

II.3.1 Rayleigh Instability

Rayleigh instability is a surface tension driven break down of a liquid jet column that features the inception and growth of one primary wavelength in the jet column. For Re<2000 and P*>0.1, a microscale liquid butane jet, formed from the same orifice described in section II.2, experiences disturbances distorting the cylindrical shape of the column and eventually breaking up the jet. The evolution and disintegration of a 10 μm jet column is shown in a sequence of images in Fig. II.3. Each image shows a 10 diameter segment of the jet at four streamwise directions (x/D=2, 100, 200, 216) for Re=800, P*=0.25. From left to right, the images show an initially disturbed jet column following formation to a cylindrically smooth that eventually develops surface waves and finally breaks up into droplets. The initial instability at the exit of the nozzle (Fig. II.3a) is apparently caused by the internal flow within the nozzle. It appears under these flow conditions, at x/D=100, these disturbances are attenuated and the column becomes cylindrical (Fig. II.3b). At x/D;200, surface waves appear on the jet column (Fig. II.3c). These waves are amplified and ultimately the jet breaks up into droplets (Fig. II.3d), Two types of droplets are formed: planetary droplets which have diameters on the order of the jet diameter and satellite droplets which have diameters much smaller than the jet diameter. The disintegration of microscale and macroscale jets appear to behave similarly because the wavelengths of break up for 10 μm approach the predicted λ/D=4.5 (Rayleigh, 1894) and the production of satellite droplets are also observed in macroscale jets (Goedde and Yuen, 1970). The remainder of the chapter discusses the evolution of the 10 μm jet column, the break up distance as *Re* and P^* changes, the formation of planetary

and satellite droplets, and the droplet wavelength as .*Re* and P^* changes. The findings from each of these sections show that a 10 μm butane jet breaks up similarly to macroscale liquid jets.

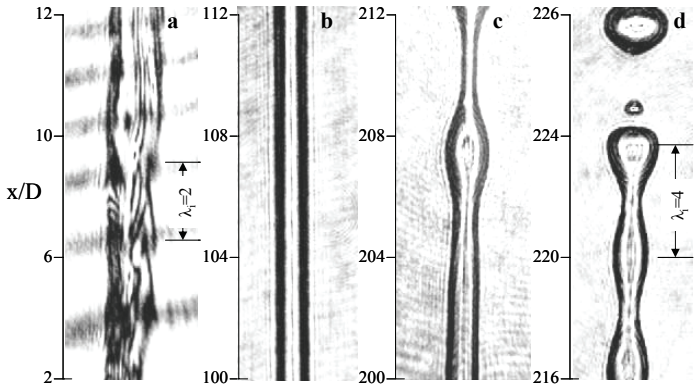

Figure II.3: *Butane Jet Image Re=800, P^*=0.25 a) x/D=2, b) x/D=100, c) x/D=200, and d) x/D=216.*

As shown in Fig. II.3a, near the exit plane the jet appears to be disturbed by the flow within the nozzle that have a nominal λ_i/D=2. These disturbances may arise from: cavitation, flow separation, wakes or shearing stress on the nozzle wall. Cavitation does not occur because computations show that the jet pressure never reaches the vapor pressure of liquid butane. Additionally, Hiruyasu, Arai, and Shimizu (1991) show that the formation of a cavity in a smooth nozzle with a 3 mm diameter would form an atomized spray jet. Wu et al. (1983) show that convergent nozzles do not tend to have cavitations. Flow separation and wakes do not occur in convergent nozzles with a smooth edged entrance as the one used in the present work. Therefore, the disturbances that appear in the emergent jet column must arise from shearing stress on the nozzle wall and asymmetric orifice geometry. Hiruyasu et al. (1991) show that wall friction (the shearing stress the wall exerts on the fluid) can create minor disturbances in the jet column at the exit of the orifice that eventually decay farther downstream. This behavior is observed in the 10 μm jets studied at high magnification images, for which butane was chosen as the test liquid. Once the jet leaves the orifice it experiences a strong decrease in shear stress since the shear stress at a liquid-air interface is negligible compared to liquid-solid interface upstream of the nozzle. While surface tension reshapes the cross-section of the jet, viscosity dampens the disturbances induced within the nozzle, allowing the jet to form an undisturbed circular cross-section (Fig. II.3b). Kasyap et al. (2008) show water jets [*O*(1 mm)] that emanated from elliptical orifices produced jets with varying cross-section in the streamwise direction. Their work shows how surface tension forces restore the jet to circular cross-section. However surface tension drives the jet to develop symmetric surface waves and finally break up.

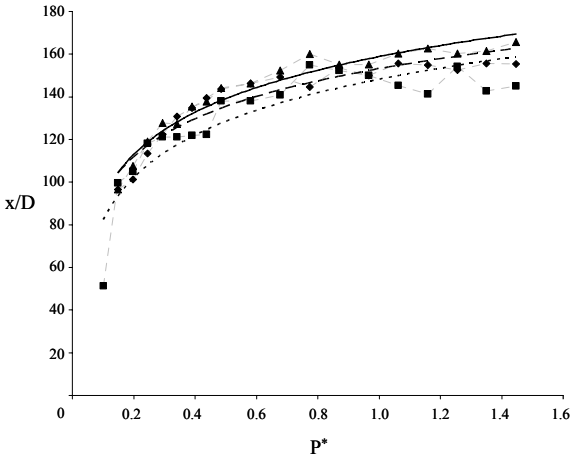

Figure II.4: *Variations of break up distance with P^* for Re= 800(♦), 1100(■), and 1400(▲).*

The jet break up distance is defined as the length of the jet column from the orifice to the point of droplet pinch off. The break up distance is discussed here for a 10 μm liquid butane jet for 800<*Re*<1400 and 0.1<P^*<1.6. The break up distance changes very little over the range of *Re*. This behavior may be due to the adverse effects of the noncircular orifice discussed previously. However, over the range of P^*, the break up distance does vary and may be due to evaporative cooling that reduces the jet liquid temperature and surface tension.

In a series of measurements, P^* was varied for 3 jet Reynolds numbers. It was found that, for $P^*<0.7$, the break up distance increased with P^*. However, it appears that when $P^*>0.7$, the break up distance becomes invariant with P^*. That is, once the ambient pressure approaches the vapor pressure of the jet fluid, the break up distance becomes insensitive to ambient pressure, because evaporation cools the liquid jet and increases surface tension. Kowalewski et al. (1993). observe similar increases in break up distances of 0.2 mm ethanol jets with increasing ambient pressure (P>20 kPa or $P^*>3.4$) claiming the formation of a cold viscous layer on the surface of the jet affected the break up. The differences between their observations and the ones made in the present work may be attributed to differences in jet diameter, which may change the ambient pressure needed to cause this trend in break up distance. Their experiments also show a dramatic increase in the ethanol jet break up distance when the ambient pressure is reduced below 20 kPa, which was not observed in the present work most likely due to the initial disturbance that is caused by flow within the nozzle.

The breakup of the jet column as a result of Rayleigh instability leads to the formation of droplets (Fig. II.5). There are two primary droplet scales namely, planetary droplets that scale with jet diameter and satellite droplets that have a diameter typically around 0.1D. The formation of planetary droplets from a jet column initiates as a swell of liquid (Fig. II.3d), that grow into a bead connected by a thin ligament of fluid (Fig. II.5a). The internal pressure is greater in the ligaments than in the swell of the jet column due to the ligament having smaller radii of curvature (Goedde and Yuen, 1969). Therefore, surface tension force increases with decreasing diameter induces an adverse axial pressure gradient that leads to fluid flow from the thin ligaments of the jet into the thicker swells. Eventually the droplet pinches when the ligament is too thin to sustain any mechanical loading (Fig. II.5b). The ligaments (that the planetary droplets pinch off from) may pinch off as well form satellite droplets or recede into the jet column. If the ligament recedes, its tip becomes rounded and then is absorbed into the upstream swell (Fig. II.5). After pinching off, the droplets travel downstream at a velocity of 10 m/s and undergo vibrational modes (Fig. IV.5), which are eventually dampened by viscous forces and the droplet become spherical, by surface tension forces.

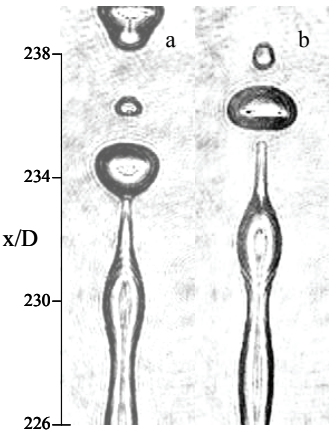

Figure II.5: *Detachment of a droplet at Re=800 and P^*=0.25, a) and b) are 1 μs apart.*

The ligaments that pinch from the jet column develop into satellite droplets (Fig. II.6). These ligaments do not recede back into the jet column, but instead develop an internal swell as a result of the necking at both ends and pinch under surface tension forces. Once detached, these ligaments contract further and finally form a spherical droplet. Some of these satellite droplets continue to travel at about 10 m/s while other slower satellite droplets merge with the faster moving, larger planetary droplets (Fig. II.6). The satellite droplets have lower velocity because pinching off and recession of the ligament into the body of the ligament occur earlier in the head, than in

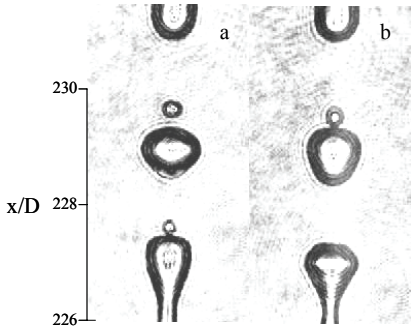

Figure II.6: *Absorption of satellite droplets at Re=800 and P^*=0.25, a) and b) are 1 μs apart*.

the tail, allowing surface tension to accelerate more mass in the direction opposing the flow, and thereby reducing the overall momentum. Fig. II.6 shows a satellite droplet traveling about 8 m/s. These mechanisms are discussed by Goedde and Yuen (1970) who investigated the formation of satellite droplets from 4mm water jets triggered by acoustic disturbances. As shown by Pimbley (1975), the formation of satellite droplets along with planetary droplets indicates a non-linear break up. A linear break up involves the necked region progressively thinning until pinching occurs in the center of the necked region and not at the extremities of connecting ligaments as predicted by Lord Rayleigh (1879). The planetary droplets are the result of this linear break up. The appearances of satellite droplets, which evolve from ligaments that pinch at their extremities, indicate the instabilities at wavelengths less than the one predicted by Rayleigh's linear stability analysis.

The variation of the wavelengths with P^* indicates no specific trend. Averaging over the range of P^*, shows that 95% of the data is within 2σ of the average. However, *Re* does appear to affect the droplet wavelength . There appears to be a decrease in wavelength as *Re* increases (as the jet speed increases). For $Re<500$, $\lambda/D;4.5$, as predicted by Rayleigh (1879). It is conjectured that this decrease is associated with the increased effect of the disturbances that are induced by the nozzle. The fact that the rate of the decrease diminishes indicates transition from Rayleigh break up to sinuous instability (Section II.3.2).

II.3.2 Sinuous Instability and Break up

Sinuous instability is the instability of the jet column that involves undulation of the jet column and the appearance of a ruffled surface throughout the entire length of the column. Early investigators of jet break up phenomena observed these column instabilities (Rayleigh, 1879 and Smith and Moss, 1916). The instability tends to be driven by disturbed flow from the nozzle that has not settled and aerodynamic drag on the jet column. The factors that contribute disturbances from these two mechanisms on the jet are nozzle geometry and roughness, liquid properties (e.g. viscosity, density), and the ambient atmosphere characteristics (e.g. air velocity, density). As mentioned before, the present nozzle has a channel surface roughness of 0.005D. Ida, et al. (2002) compare two 10 mm nozzles with different surface roughness: 0.0006.3D and 0.01D. They find that the rougher nozzles formed jets with larger surface rippling, one of the main features of sinuous instability. They also show that these surface ripples grow with jet speed. Brown and York (1966) report the effects of surface roughness on the break up of cold water jets by comparing two types of nozzles [O(0.5mm)]. They report that the jet formed by a nozzle with roughness 0.0004D formed a jet column with a rippled surface and the jet formed by a nozzle with roughness 0.12D simply atomization immediately downstream of nozzle. The disturbances from the flow in the nozzle and aerodynamic drag in the ambient atmosphere can be affected by the jet liquid properties (e.g. viscosity, surface tension Characteristics of the ambient atmosphere affect the jet because higher density increases the aerodynamic drag on the jet and also introduce atmospheric turbulence. Kerst, et al. (2000) show the transition from Rayleigh instability to sinuous instability by increasing the ambient pressure. In the present work, butane jets formed at the minimum and maximum *Re* and P^* are examined to show the role each parameter plays in the formation of the jet column and ultimate break up of the jet. They showed that the transition to sinuous instability appears with a sudden decrease in break up distance and affects the evolution of droplets.

As noted above, the transition of a liquid jet from Rayleigh instability to sinuous instability is manifested by the appearance of wavy undulations on the jet column. Fig. II.9 is a compilation of high resolution images of five jets imaged in four windows (height of 30D) that have been stitched together. Each jet in Fig. II.7 is chosen to illustrate the differences between Rayleigh and sinuous instability and the evolution of sinuous instability over *Re* and P^*. Sinuous instability can be observed in a) *Re*=1790 and P^*=0.29, b) *Re*=1790 and P^*=1.45, c) *Re*=2950 and P^*=0.29, and d) *Re*=2950 and P^*=1.45. The jet in e) *Re*=800 and P^*=0.29 breaks up from Rayleigh instability and differs from the other four jets in its apparently smooth jet column. Comparing a) and b) where P^*=0.29, the jet appears to be slightly more disturbed for the increased *Re*. Comparing c) and d) where P^*=1.45, the jet column is greatly disturbed for the increased *Re*. Comparing a) and c) where *Re*=1790, the jet column appears slightly more disturbed for increased P^*. Comparing b) and d) where *Re*=2950, the jet column is greatly disturbed with increased P^*, especially after *x/D*>80. This increased disturbance with both *Re* and P^* because they both affect mechanisms that cause sinuous instability. Increases in *Re* .amplifies disturbances originating in the nozzle and increases the likelihood liquid jet turbulence upstream and downstream of the orifice exit. Increases in both *Re* and P^* increases both the aerodynamic drag and the likelihood of turbulence in the atmosphere. Kerst et al. (2000) define a transition that is dependent on *Re* and P^*. Their transition agrees with the conjecture that increases in both *Re* and P^* increases transition to and the disturbances caused by sinuous instability.

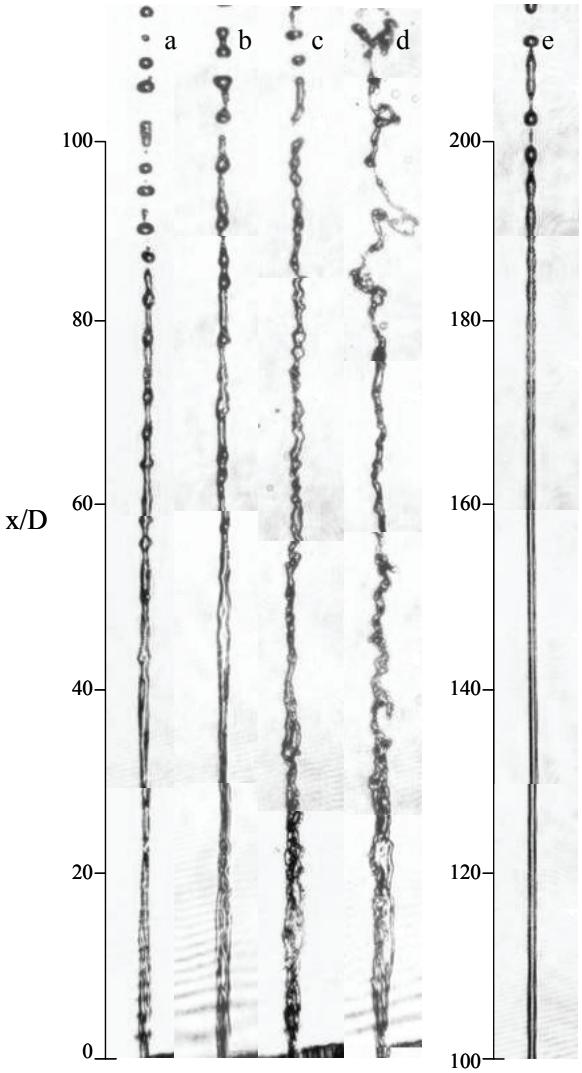

Figure II.7: *Butane Jet evolution and break up at a) Re=1790 P^*=0.29, b) Re=1790 P^*=1.45, c) Re=2950 P^*=0.29, d) Re=2950 P^*=1.45, and e) Re=800 P^*=0.29*

The trend of the break up distance of the liquid butane jet with sinuous instability shows two significantly different features (Fig. II.8). First, the break up distance decreases when the jet transitions from Rayleigh to sinuous instability for constant P^*. This is because the disturbances that originate from flow within the nozzle are not attenuated for Re>2000, are propagated downstream, and are amplified by the aerodynamic drag and atmospheric interaction. Grant and Middleman (1966) and McCarthy and Molloy (1974) discuss this critical point where the jet break up distance rapidly decreases when the jet transitions from Rayleigh instability to sinuous instability. Second, there is a gradual increase in break up distance with P^*.from its minimum

value. This behavior is analogous to the discussion in Chapter II.3.1, where jets under Rayleigh instability broke up closer to the orifice when P^*.is reduced.

Droplet formation as a result of the sinuous instability is characterized by the formation of a broad distribution of irregularly shaped droplets. Comparing Fig. II.9a and II.9b, the droplets in a) are more regular and in b) the jet produces strands of droplets that appear to be droplets connected by ligaments. The differences are that in a) the jet is still breaking down from surface tension, even though sinuous instability affects the jet column and in b) the sinuous instability mechanically breaks strands of liquid off the jet column before individual droplets can pinch off., which was discussed by Grant and Middleman (1966). Fig. II.10 (x/D=200) shows the droplets farther downstream from the break up distance. The stream of droplets in Fig. II.10a and IV.10b appear much more similar than those of Fig. II.9a and b. The strands of liquid apparently break up at the thin ligaments that connected droplets in Fig. II.9b, presumably driven by surface tension. The wavelengths appear different and in Fig. II.8, the wavelength was shown to decrease with increasing *Re*. The snapshot in Fig. II.10 can be mislead since the wavelength appears to increase with *Re*.

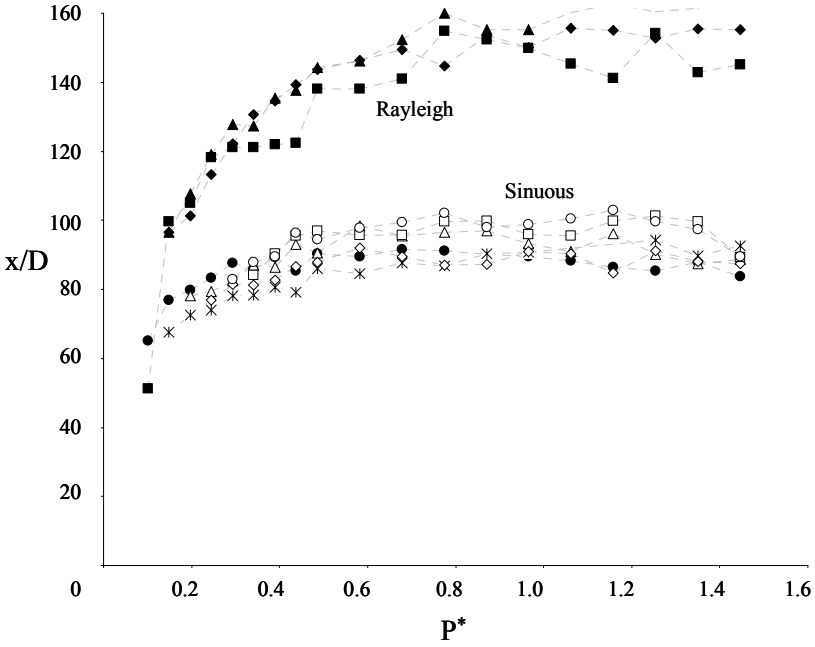

Figure II.8: *Break up distance over dimensionless pressure, Re= 800(♦), 1100(■), 1400(▲), 1800(●), 2030( ), 2300(Δ), 2430(◊), 2710(□), and 2950(○).*

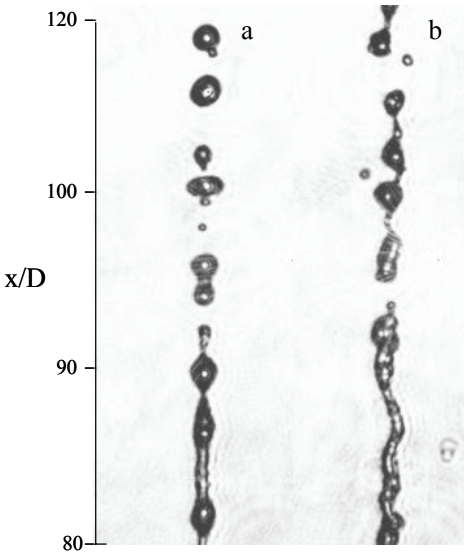

Figure II.9: *Sinuous instability break up for P^*=0.29 at Re= a) 1790 and b)2950*

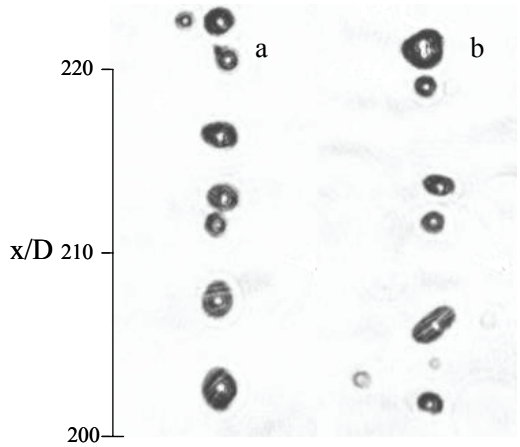

Figure II.10: *Sinuous instability break up for P^*=0.29 at Re= a) 1790 and b)2950*

Varying P^* affects droplet features and evolution, but the variation is dependent on the magnitude of *Re*. For *Re*=1790, a sinuous jet produces droplets in a manner that doesn't appear to depend on P^*. However comparing two jets at *Re*=2950 in Fig. II.11a at P^*=0.29 and Fig. II.11b at P^*=1.45, more

irregularly shaped droplets pinch off the jet column at larger P^*.

II.3.3 Sinuous Atomization

Sinuous atomization can be characterized as the break up of a jet due to sinuous instability into droplets which propagate in the streamwise and radial directions. The disturbances that originate from flow within the nozzle and atmospheric interaction become more dominant in breaking up the jet. This section presents is limited to the study of on case due to the limitations of the experimental set up. The difference in P^* indicates the apparent importance of aerodynamic effects, such as aerodynamic drag and air turbulence. Kerst, et al. (2000) cite two main factors that drive a jet injected into high ambient pressure to break up from sinuous instability into atomized spray. First, the higher pressure enhances gaseous interaction with the jet. Second, the gas dissolves into the jet liquid, which considerably changes the jet liquid properties. However, it is conjectured here that since the fluid of interest is a light hydrocarbon, higher pressures allow more of the fluid to evaporate into the atmosphere, and alter the atmospheric interaction with the jet.

In the present work, aerodynamic drag and possibly turbulence of the ambient atmosphere introduce asymmetric disturbances which cause the formation of ligaments pulled from one side of the jet column that ultimately pinch and break up into droplets. In Fig. II.12, image a) and b) are 1 μs apart and show the evolution of a ligament. The ligament may be initiated by disturbances that originate in the nozzle and may be like those of Hoyt and Taylor (1977). They attribute the atomization of their 6.35 mm water jets to turbulence and the formation of hair pin vortices within the jet column (initiated by disturbances originating from flow within the nozzle) that produces ligaments that protrude from the jet column and ultimately they claim surface tension causes droplets pinching from these ligaments. Fig. II.13 shows a similar break up of a butane jet that develops a protruded ligament and has begun to pinch droplets.

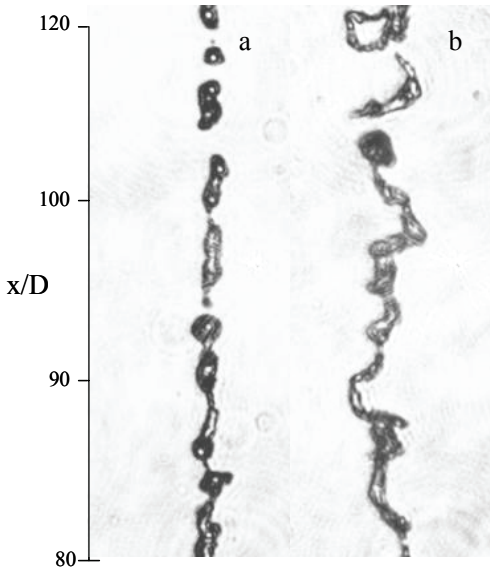

Figure II.11: *Jet column at Re=2950 a) P^*=0.29 and b) P^*=1.45*

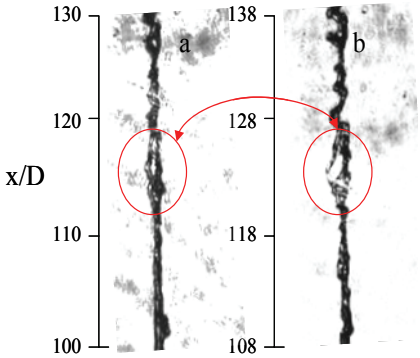

Figure II.12: *Two frames 1μs apart showing the formation of a liquid thread. Re=2950 and P^*=1.93.*

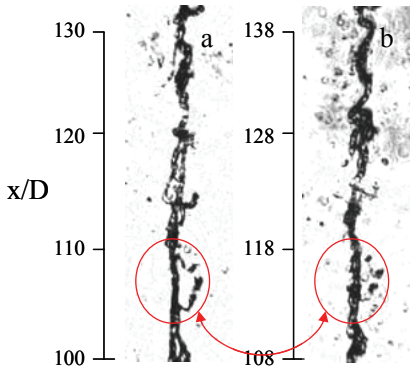

Figure II.13: *Two frames 1 μs apart showing the break up of the thread into distinct droplets.*

II.3.4 Evaporation Instabilities

As mentioned previously, evaporative instability is driven primarily by evaporation from the jet surface. Asymmetric evaporation from the jet column surface introduces surface tension gradients that give rise to Marangoni forces that affect the jet column, usually creating bending jets or stabilizing film structures. Additionally, evaporation can create vapor pockets and branching jets through the vapor recoil effect and Marangoni forces. Typically, these effects are observed for Re<800 and P^* <0.1, although other investigators, such as Kowalewski et al (1993) have observed evaporative instabilities up to P^*=1.

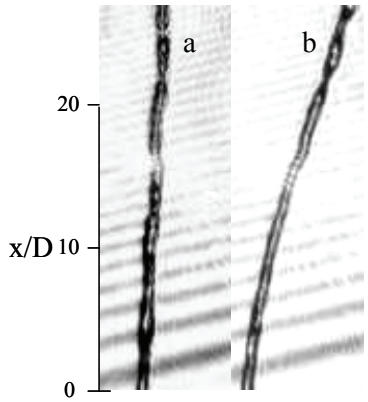

Figure II.14: *Jet under reduced ambient pressure Re= 1380 and P^*=0.07.*

Jet bending is a phenomenon where a straight jet column will curve due to the Marangoni effect. Kowalewski, et al. (1993) determine that the Marangoni effect caused their 1 mm ethanol jets to bend due to asymmetric evaporation. They also determine that once the jet column bends, the lateral circulation, caused by the Marangoni effect, enhances the evaporative cooling preferentially on one side of the cylinder, which creates larger surface tension gradient. The asymmetry of the nozzle orifice in the present work causes the jet column cross-section to be asymmetric and the jet bends due to non-uniform evaporation cooling the jet non-uniformly. This causes asymmetric thermodynamic properties (specifically surface tension) resulting in the bending of the jet column (Fig. II.14). The effect is sustained by constant P^* reduced to the point the ambient pressure drives steady evaporation. There are two main differences between the jets discussed in Kowalewski, et al. (1993). The first difference is that the jet required 60D to bend, whereas the asymmetry in the emerging jet in the present work causes very early bending in the jet. This is probably the result of the asymmetry of the initial jet column in this experiment compared to Kowalewski's jets. The second difference is that the bending jets obtained here were extremely stable, maintaining a consistent bend, while the jets of Kowalewski could only remain bent for a few seconds, which is related to the length scale of the respective jets.

Hollow-cone formation and branching occurs when the vapor pocket disturbs the jet such that the jet column will split into two or more branches. For P^*=0.065 and Re=500, the vapor pocket no longer disappears, but still oscillates from a trapped vapor pocket to a hollow-cone state (Fig. II.15a to IV.15e). In the closed state, the jet branches encapsulate a vapor pocket. In Fig. II.15c to IV.15f, the jet vapor pocket opens into a hollow-cone structure creating individual branches connected by liquid film and each branch appears to break down due to Rayleigh instability.

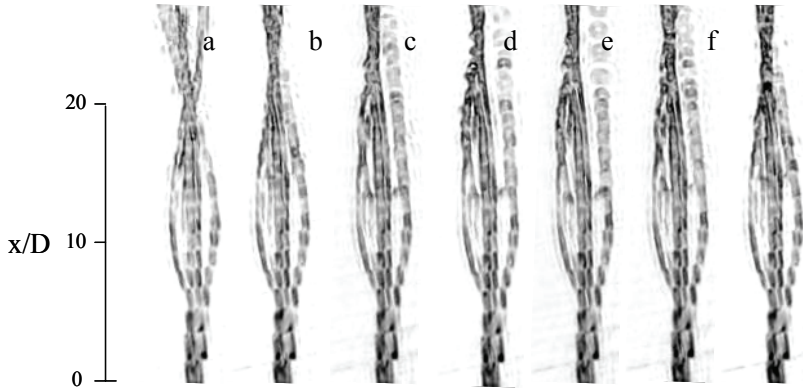

Figure II.15: *Jet branching under reduced ambient pressure Re= 500 and P^*=0.065.*

The oscillating behavior may arise from two sources. The first source of fluctuation in state is owed to varying local pressure which varies the rate of evaporation affecting the fluctuations in the jet column temperature and other thermodynamic properties such as surface tension. The varied rates of evaporation cause variation in the "vapor recoil" effect which creates the hollow cone structure. "Vapor recoil" is an effect of additional pressure on a liquid surface due to evaporation from that liquid's surface (Palmer, 1976). Kowalewski et al. (1992) determine this effect causes the formations wings on evaporating ethanol jets injected into an evacuated environment. They reason vapor recoil increases surface area, enhancing the evaporation and increasing the instability. However, in the present work, the jets tend to close once they attain the maximally hollow-cone state, thus the additional pressure from vapor recoil is only sufficient to create a marginally stable jet configuration, one that oscillates in this fashion, but never reverts to a column nor full splaying. The second possible source of the oscillatory behavior is the evaporative effects itself. Although the reduced pressure does drive the evaporation, the evaporative system can be naturally oscillating. When evaporation occurs, vapor recoil happens, the jet acquires greater surface area and the jet liquid surface cools. If the evaporation is sufficient to create enough vapor recoil then the jet opens further allowing more evaporation and cooling of the jet surface. Yet when the jet liquid surface cools locally, heat is conducted into that location, resulting in jet cooling in neighboring locations. Since the liquid is cooler, evaporation is reduced with the effects of vapor recoil. Sufficient weakening of vapor recoil will allow the jet to close since the local pressure within the hollow cone is reduced.

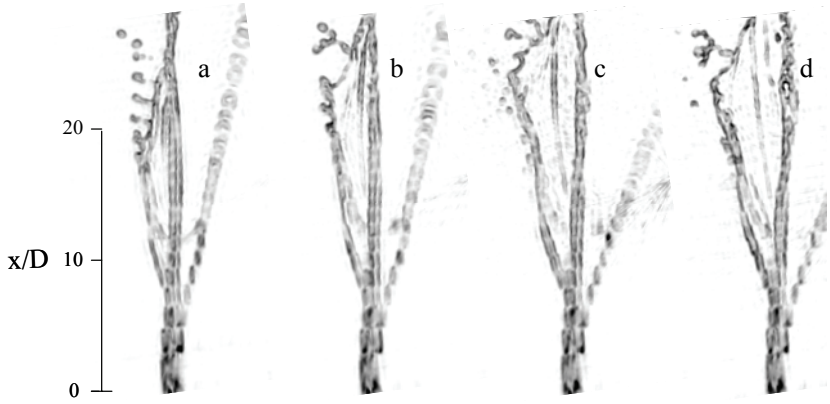

Figure II.16: *Jet branching under reduced ambient pressure Re= 500 and P^*=0.05.*

The jet establishes stable branches P^*<0.05 driven by evaporative cooling, vapor recoil, and the Marangoni effect. The branches are connected by liquid film (Fig. II.16). The jet branches appear to break up into droplets similar to Rayleigh jets. The film in between branches

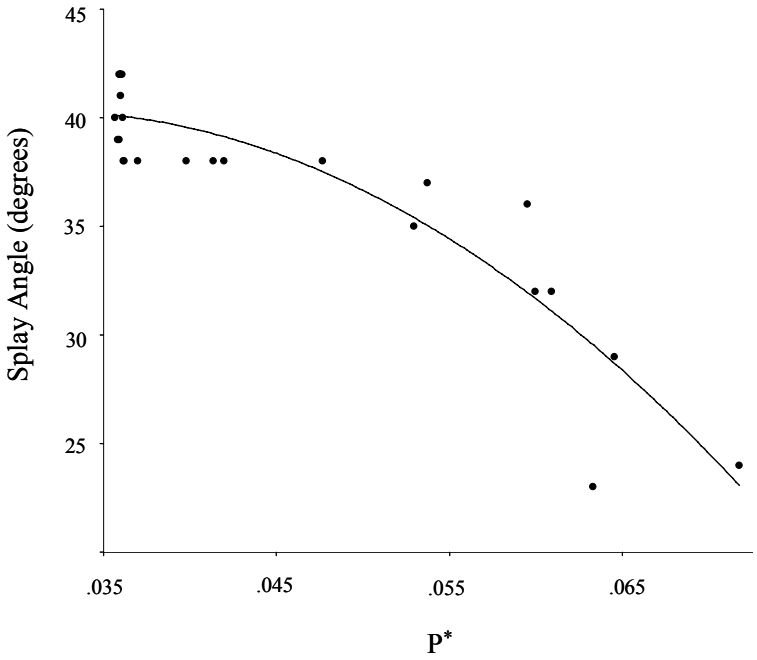

Figure II.17: *Splay angle versus P^*, Re=500.*

breaks down shedding ligaments. This form of shedding of ligaments does bear some similarity to traditional break up of liquid sheets (Chigier, 1991). However the mechanism that initiates ligament shedding from the liquid film is different. The break up of the far left branch of the jet in Fig. II.16a-d appears to pull liquid from the film boundaries, causing the film to shed a ligament. This hollow-cone structure may be similar to "wings" and film structure produced by ethanol and ether jets formed by Kowalewski et al. (1995). The ethanol jet developed stable "wings" which appeared to be a cup opening which had liquid film skin. The "wings" appear to shed off ligaments in much the same manner. The film formed from ether-ethanol jets and is enveloped by two veins, much like the film formed in Fig. II.16a. Kowalewski did not indicate if the film broke similarly to the film structures here, but they did show films that formed surface waves, which appears in Fig. II.16 as ruffles.

The splay angle, the relative angle between two visible branches, of the jet at this point is a function of P^* (Fig. II.17). The jet branches gradually splay further with decreasing ambient pressure, finally reaching a point where the trend accelerates, indicating the onset of jet flashing. The increases in the splay angle are driven by increased evaporation and vapor pressure inside the hollow-cone of the jet.

II.3.5 Flashing Instability

Flash evaporation or flashing instability is break up of a liquid jet into segmented liquid threads or spray caused by the formation and rupture of vapor bubbles. In the present work, this instability occurs at $P^*<0.08$ and for $Re>1000$ or $P^*<0.03$ and for $Re<1000$. There are three manifestations of flashing instability: segmented column, atomized spray, and unstable branching.

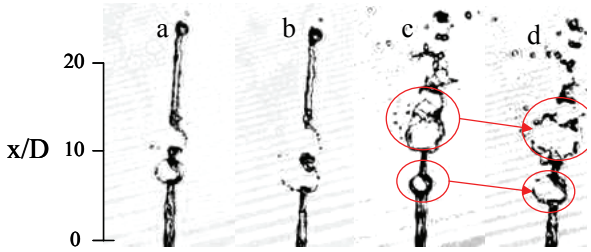

Figure II.18: *Butane jet with vapor bubble Re=1100 and P^*=0.077; a) and b) are 1 μs apart show the segmented column; c) and d) are 1 μs show the jet is on the verge of spray*

The jet column is segmented when infrequent vapor bubbles form and rupture (Fig. II.18a and IV.18b). The frequency of vapor bubble formation increases during the same experiment due to fluctuations and the small scales involved. The jet column oscillates between breaking into segments by infrequent vapor bubble ruptures and breaking into a spray when the bubble formation and rupture occurs more frequently (Fig. II.18c and IV.18d). The vapor bubble ruptures in Fig. IV.18c and IV.18d destroy any column segments by rapidly expanding into undisturbed columns and then the violent vapor bubble rupture adds disturbances to the remaining undisturbed segment, breaking it down into droplets. Lienhard (1966) illustrates these two forms of flashing break up. He points out that if the velocity of the explosion is greater than the jet velocity then the jet will be segmented liquids and if not a spray will form. In Fig. II.18, the mode of the break up oscillates between the two configurations because of small fluctuations in local pressure in the ambient medium and fluctuations in the jet liquid temperature all due to the small scale of the experiment. Furthermore, roughness of the nozzle, nozzle diameter, and liquid properties adds to the variability of nucleation sites, making vapor bubble formation more random. This effect is discussed by Brown and York (1962) when comparing rough and smooth nozzles. The emergent jet column is greatly affected by the roughness of the present nozzle. Vapor bubbles that may nucleate at arbitrary sites are warped and randomly redistributed as the jet column evolves with

an initially distorted cross-section and abnormal velocity distribution. This process promotes irregular vapor bubble growth and rupture, also aiding in oscillations between segment liquid threads and spray.

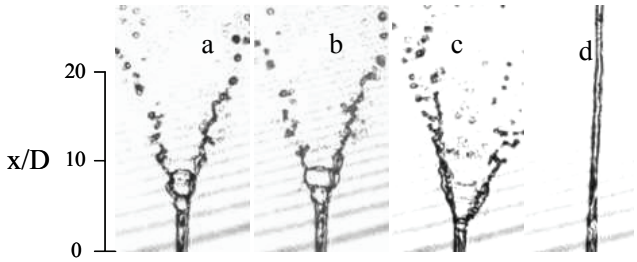

Figure II.19: *Butane jet with vapor bubbles forming and rupturing causing unstable bifurcation Re=1100 and P^*=0.077.*

Flashing jets can also momentarily branch due to vapor bubble formation and rupture, which splays the jet column. The splaying is not stable since the vapor recoil is insufficient to stabilize the splay (Fig. II.19). This weak interaction from the rupture of a vapor bubble is one of the ways a branched jet may initiate. The appearance of the vapor bubble is accompanied by evaporative cooling of the fluid around the bubble, which temporarily sustains the splay in the jet. However, the configuration is not sustained and reverts to a column jet. The time length of the splaying is also unknown because of the limitations of the equipment.

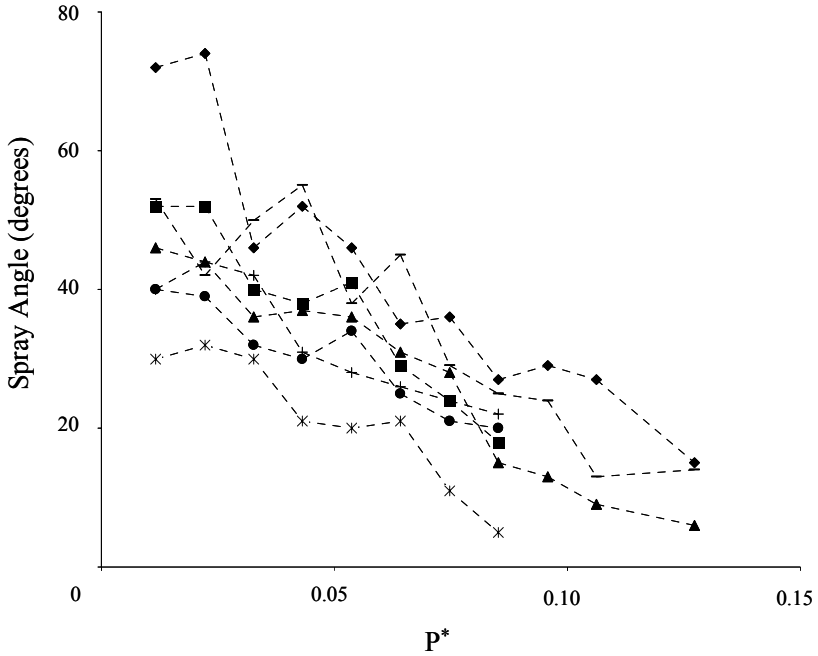

Figure II.20: *Spray angle versus P^*, Re= 3450(♦), 4060( ), 4160(▲), 4870(■), 5120(*), 5480(●), and 5480(+).*

Spraying jets evolve from the orifice as fine droplets that spread from the jet centerline. P^* drives the rate of the bubble nucleation and growth rate. Chaves et al. (1988) describe the behavior of the vapor bubbles and void fractions within the jet as being in mechanical disequilibrium with the ambient pressure. This can imply greater disequilibrium increases the spray angle. This behavior is observed when decrease in P^* increases the spray angle of the jet (Fig. II.20). The formation, growth, and destruction of the vapor bubbles are so energetic that the jet is atomized into fine droplets (Fig. II.21a). Spray angle trends of lower *Re* tend to occur above trends of higher *Re* (Fig. IV.20). Some irregularities in a few trends exist where the *Re* increases and the spray angle unexpectedly increases, but this is an anomaly probably caused by the present nozzle geometry. The increase in spray angle with decreasing *Re* is expected because the sine of the angle of the jet is the ratio between jet velocity which increases with *Re*

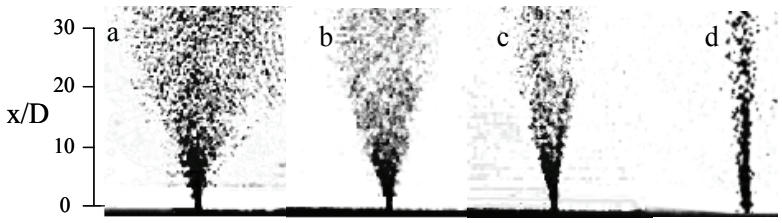

Figure II.21: *Spraying propane jet Re=4160 and P^* = a) 0.012, b) 0.043, c) 0.075, and d) 0.103.*

and radial expansion of the spray jet, which is driven by the bubble formation and rupture.

In Fig. II.21, the column jet begins to appear as the P^* increases and the spray angle is reduced by less disequilibrium. Further increase in the P^* will establish a column jet that breaks up from Rayleigh instability or sinuous instability. Fig. II.21d shows a jet column which is starting to form. At Re=4160 and P^*=0.103, the jet may be atomizing both from flashing instability and possible sinuous atomization. Chaves et al. (1995) determine that turbulence occurred at about the same injection pressure as transition to cavitation (the point at which they observe bubble formation and rupture in the free jet). Their set of experiments shows that there is a range of Re and P^* where both processes atomize the jet. Finally, Fig. II.22 shows a transition map in Re and P^* plane that summarizes the boundaries between the various column instabilities discussed in the previous sections.

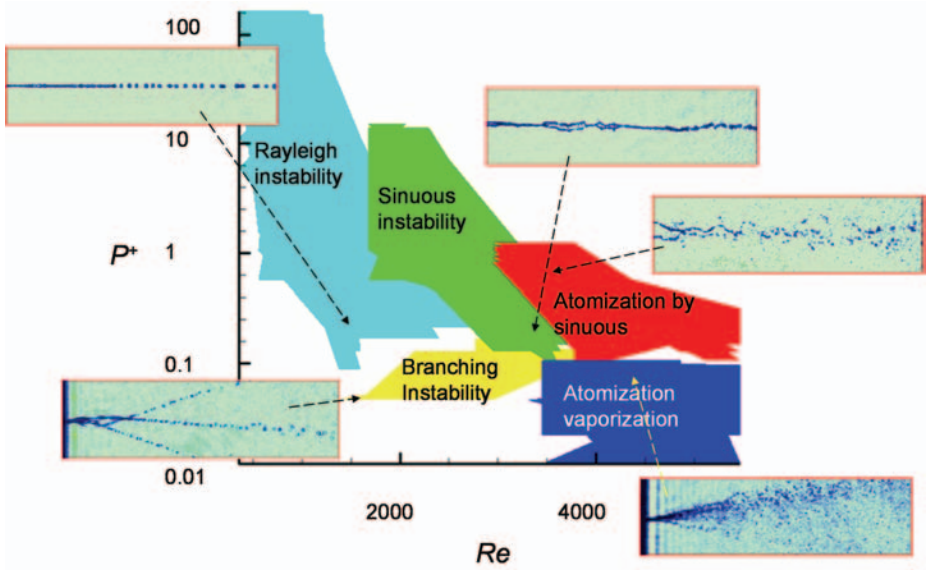

Figure II.22: *Instability maps as a function of Reynolds number and Pressure Ratio.*

References

1. McCarthy, M. J. and Molloy, N. A., "Review of Stability of Liquid Jets and the Influence of Nozzle Design," *The Chemical Engineering Journal*, **7**,1-20, 1974.
2. Kusui, T., "Liquid Jet Flow into Still Gas," *Japan Soc. Mech. Eng.*, **11**, 1084-1090, 1968.
3. Goedde and Yuen, "Experiments on Liquid Jet Instability," *J. Fluid Mech.*, **40**, 495-511, 1970.
4. Beggenir, "The Role of Orifice Design in Hydroentanglement", MS Thesis, North Carolina State University, 2002.
5. Lin, S. P., **Breakup of Liquid Sheets and Jets**, Cambridge University Press, 2003.
6. Lasheras, J. C., and Hopfinger, E. J., "Liquid Jet Instability and Atomization in a Coaxial Gas Stream," *Annu. Rev. Fluid Mech*, **32**, 275-308, 2000.
7. Meister, B. J., and Scheele, G. F., "Drop Formation from Cylindrical Jets in Immiscible Liquid Systems," *AlChE Journal*, **15**,700, 1969.
8. Drazin, P. G., and Reid, W. H., **Hydrodynamic Stability**, Cambridge University Press, 1991.
9. Brown, R., and York, L., "Sprays Formed by Flashing Liquid Jets," *AIChE Journal*, **8**, 149-153, 1962.

10. Charwat, A. F., and Russali, R. R., "On the disintegration of Superheated Capillary Jets," *PhysicoChemical Hydrodynamics*, **2**, 55-60, 1981.

11. Chaves, H., Knapp, M., Kubitzek, A., Obermeier, F., Schneider, T., "Experimental Study of Cavitation in the Nozzle hole of Diesel Injectors Using Transparent Nozzles," *SAE Paper*, **950290**, 199-211, 1995.

12. Chaves, H., Kowalewski, T. A., Kurschat, T., Meier, G. E. A., and Müller, E. A., "Similarity in the Behavior of Initially Saturated or Subcooled Liquid Jets Discharging Through a Nozzle," *Chemical Physics*, **126**, 137-143, 1988.

13. Chigier, N. A., "The Physics of Atomization," *ICLASS-91*, 1-15, 1991.

14. Kasyap, T. V., Sivakumar, D., and Raghunandan, B. N., "Breakup of Liquid Jets Emanating from Elliptical Orifices at Low Flow Conditions," *Journal of the International Institutes for Liquid Atomization and Spray Systems,* **18**, 645-668, 2008.

15. Kerst, A. W., Judat, B., Schlünder, E. U., "Flow Regimes of Free Jets and Falling Films at High Ambient Pressure," *Chemical Engineering Science*, **55**, 4189-4208, 2000.

16. Lienhard, J. H., "An Influence of Superheat Upon the Spray Configurations of Superheated Liquid Jets," *Transactions of ASME*, **88**, 685-687, 1966.

17. Lienhard, J. H., and Day, J. B., "The Break Up of Superheated Liquid Jets," *Transactions of ASME: Journal of Basic Engineering*, **92**, 515-521, 1970.

18. Hiroyasu, H., "The Breakup of High Speed Jet in a High Pressure Gaseous Atmosphere," *Proceedings of the 2nd International Conference on Liquid Atomization and Spray Systems*, 69-74, 1982.

19. Hiroyasu, H., "Spray Breakup Mechanism from the Hole Type Nozzle and Its Applications", *Atomization and Sprays*, **10**, 511-521, 2000.

20. Hiroyasu, H., Arai, M., Shimizu, M., "Breakup Length of a Liquid Jet and Internal Flow in a Nozzle, *Proc. ICLASS-91*, 123-133, 1991.

21. Hoyt, J. W., and Taylor, J. J., "Turbulence Structures in a Water Jet Discharging in Air," *The Physic of Fluids*, **20**, S253-S257, 1977.

22. Wu, K.-J., Su, C.-C., Steinberger, R. L., Santavicca, D. A., and Bracco, F. V., "Measurements of Atomizing Jets," *Journal of Fluids Engineering: Transactions of ASME*, **105**, 406-413, 1983.

23. Pimbley, W. T., "Drop Formation from a Liquid Jet: A Linear One-Dimensional Analysis Considered as a Boundary Value Problem," *IBM Journal of Research and Development*, **20**, 148-156, 1976.

24. Kowalewski, T. A., Hiller, W. J., and Behnia, M., "An Experimental Study of Evaporating Small Diameter Jets," *Phys. Fluids A*, **5**, 1883-1890, 1993.

25. Grant, R. P. and Middleman, S., **"**Newtonian Jet Stability," *AIChE Journal*, **12**, 4, 669-678, 1996.

III. Micro- and Nanostructures for Nanojet Characterization

III.1 Overview

The goal of this part of the project is the development of dedicated micro- and nanostructures to characterize free and impinging nanoscale jets. To this end, AFM cantilevers for high-resolution force and velocity sensing and resonant cantilevers for investigation of the mass deposition by the nanojets are investigated.

III.2 Nanojet Metrology using Heated AFM Cantilevers

Local probes that rely on the flow of heat have been widely used for nanoscale thermometry, surface topographic profiling, thermal diffusivity measurement, and surface modification. A recent development for data storage technology at IBM Research and elsewhere is an AFM cantilever with an integrated heater. One goal of the research is to use these cantilevers for metrology of nanojets fluid flow.

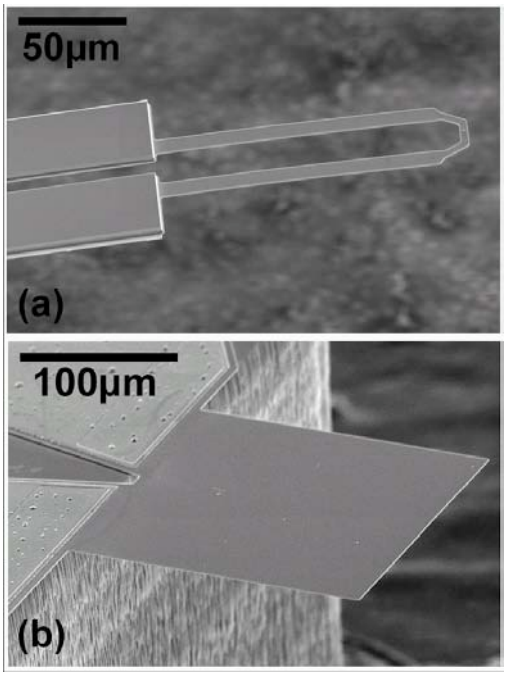

Figure III.1: *Scanning electron micrographs of (a) a U-shape heated microcantilever with a resistive heater near its free end (b) a rectangular piezoresistive microcantilever.*

Initially, the heated cantilevers were carefully calibrated. As an example, the heated cantilever shown in Fig. III.1(a) was placed into an ultra high vacuum (UHV) chamber capable of controlled pressure between 10^{-6} and 10^{3} mbar. Then, the electrical resistance of the heated cantilever was measured as a function of excitation voltage at given ambient pressure (see Fig. III.2(a)). For this cantilever, the peak electrical resistance associated with the thermal runaway corresponded to 560 °C. Two distinct pressure regimes in Fig. III.2(b) show the thermal coupling between cantilever and environment. At low vacuum, the peak resistance occurred at a decreasing excitation voltage with decreasing pressure. However, the heated cantilever became insensitive to further pressure reduction at high vacuum. Fig. III.2(c) shows the dissipated power in the cantilever as a function of the calculated mean free path or corresponding Knudsen number (*Kn*) in air when the cantilever heater temperature is held at 400 °C. There is a transition from pressure-dependence to pressure-independence of thermal conduction from the cantilever heater at approximately 2×10^{-5} m which is indeed close to the cantilever heater size. To summarize the experimental observations: at high vacuum, thermal conduction to the gas was negligible compared to thermal conduction through the cantilever legs; at low vacuum, gas conductance increased such that higher power could be dissipated at a given temperature.

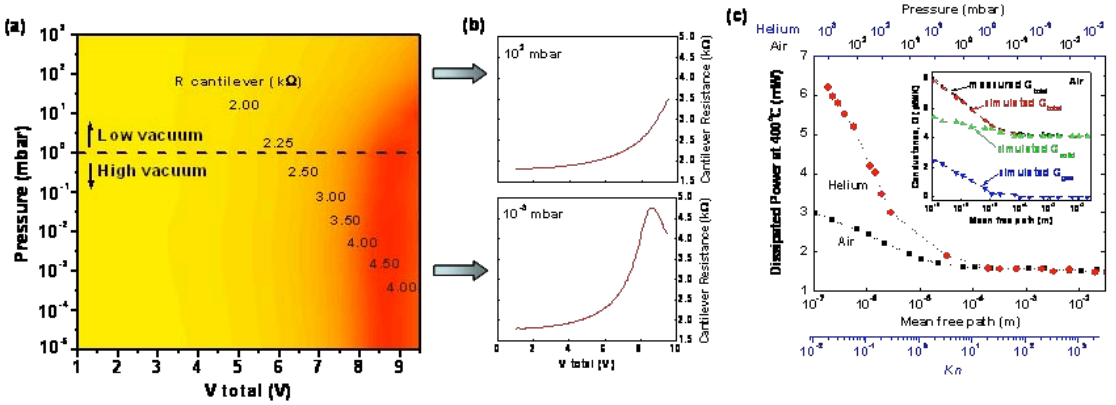

Figure III.2: (a) Contour plot of electrical resistance of a heated AFM cantilever as a function of bias voltage and pressure in air (b) Two representative plots of measured cantilever electrical resistance as a function of bias voltage at low vacuum (10^2 mbar) and high vacuum regime (10^{-3} mbar) (c) Dissipated power in a heated AFM cantilever when the heater temperature is held at 400 °C as a function of calculated gas mean free path for both air and helium. The inset shows good agreement between measured and simulated conductances with the microcantilever in air.

Gaseous nitrogen jets from a 10 μm diameter nozzle were tested with heated cantilevers. Figure III.3 shows the cantilever electrical resistance as a function of the dissipated power in the cantilever at various driving pressures. First, the electrical responses of the heated cantilever remain unchanged as long as the driving pressure is less than 1.36 MPa. As the pressure increases, the resistance (R) versus power (P) curves are shifted to higher powers such that the cantilever can dissipate more power at fixed cantilever heater temperature. At pressure higher than 8.16 MPa, the flow velocity of nitrogen jet becomes saturated and no more changes in the electrical response will be expected beyond this pressure. Since the heated cantilever is strongly sensitive to any change which affects the heat transfer, it can be inferred that the momentum of the nitrogen jet becomes negligible at pressures less than 1.36 MPa with a given separation distance (~ 700 um) between the cantilever and the nozzle. The shifted R versus P curves in the intermediate pressure ranges indicate the enhanced cooling capacity of nitrogen jets.

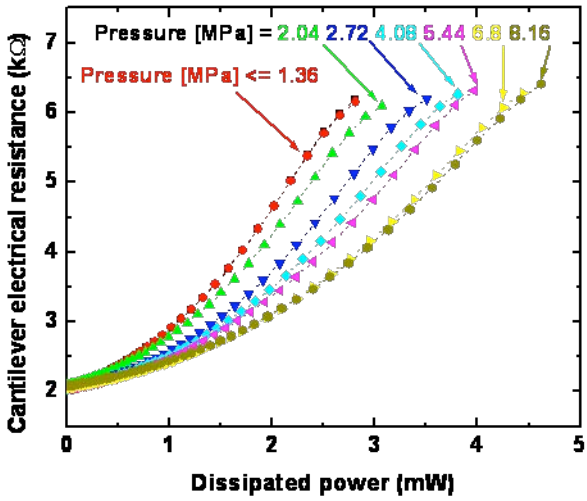

Figure III.3: Cantilever electrical resistance as a function of dissipated power in the cantilever at various gaseous nitrogen jet driving pressures where a 10 μm diameter nozzle is used with 700 μm separation between the cantilever and the nozzle.

Phase change characteristics accompanied by impinging microjets were further investigated by operating heated cantilevers (see Fig. III.1(a)) in heating and successive

cooling cycles. A custom proportional-integral-derivative (PID) controller was configured to operate them in a temperature control mode. Boiling hysteresis and boiling curve were obtained and critical heat fluxes were extracted from measurements and simulations. For all measurements, a micromachined nozzle having 10 µm diameter was used.

To investigate cooling and phase change characteristics of microjets, a heated microcantilever was aligned to and impinged upon by a butane microjet. In the previous report, cantilever power dissipation was monitored and recorded only while the input voltage was ramped up. In this Year IV of the research, cantilever power was measured during both heating and cooling cycles (see Fig. III.4). When the power dissipation was less than 4 mW or greater than 7 mW, heating and cooling curves were nearly identical. In contrast, a hysteresis was observed when power dissipation was greater than 4 mW and less than 7 mW. This hysteresis is believed to be due to the boiling on the heater surface in the microcantilever. It should be noted that voltage or power rather than cantilever heater temperature was controlled in Fig. III.4. Therefore, temperature information inside the hysteresis loop could not be obtained. Due to this hysteresis loop, the heated cantilever can have different resistance and temperature at a given power dissipation. In a voltage or power control mode, the cantilever temperature can change dramatically and the control system will become unstable.

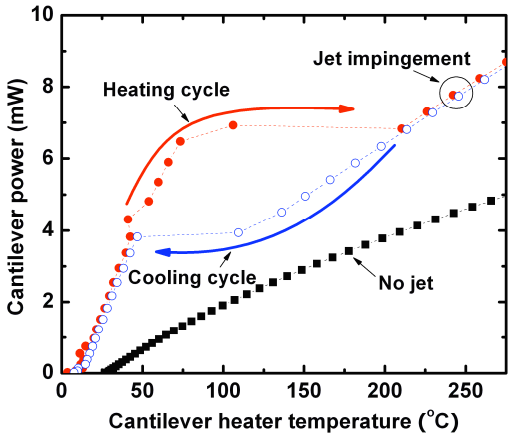

Figure III.4: *Cantilever power dissipation in an ambient air and upon a butane microjet impingement. Hysteresis exists during heating and cooling cycles. The butane jet velocity is 24 m/sec.*

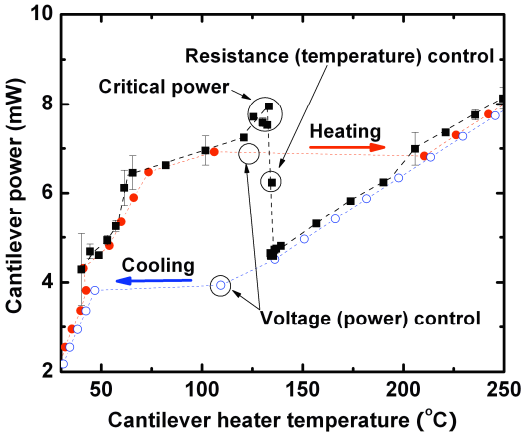

Figure III.5: *Boiling curve of the butane microjet impinging on the heated microcantilever constructed with a PID resistance (temperature) control.*

To fully construct a boiling curve, a PID controller was interfaced with the heated microcantilever and electrical resistance of the cantilever was controlled. Fig. III.5 shows the full boiling curve of the butane microjet impinging on the resistive heater in the microcantilever. In conventional boiling curves, excess temperature, $\Delta T_e = T_s - T_{sat}$, used to be on the x-axis where T_s is the temperature of the heater surface and T_{sat} is the saturation temperature at given pressure. Due to the difficulty in measuring the temperature of the liquid microjet from a 10 µm diameter nozzle, cantilever heater temperature replaces excess temperature hereinafter. From this full boiling curve, the critical power and corresponding cantilever heater

temperature were obtained. It should be noted that the transition from the nucleate boiling to the film boiling occurs within a few degrees change in the cantilever heater temperature. Without the PID control, the cantilever heater temperature suddenly increased beyond the critical power due to the vapor blanket fully surrounding the cantilever heater. Microjet cooling will be very effective near the critical power before the sudden temperature jump.

Different hydrocarbon (butane, hexane, and octane) microjets were tested, characterized, and compared in terms of the critical power. Fig. III.6 shows the cantilever power as a function of the cantilever heater temperature at various Reynolds numbers (Re). For each hydrocarbon microjet except the hexane microjets, the cantilever power is somewhat less sensitive to the jet velocity and Re at low cantilever temperatures. The anomaly of the hexane microjet is mainly attributed to the misalignment of the jet to the cantilever heater. However, increased Re extends the nucleate boiling regime and increases the critical power. After the transition from nucleate boiling to film boiling, higher power dissipation is observed at higher Re since the heat transfer coefficient increases with Re. The cantilever heater temperature corresponding to the boiling transition increases with the molecular weight of the hydrocarbon since heavier hydrocarbons (alkanes) have stronger dispersion forces which in turn increase boiling and melting points.

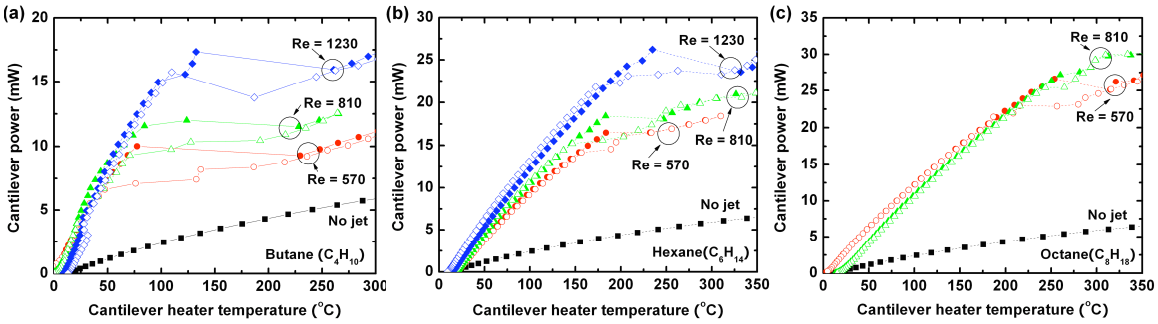

Figure III.6: *Boiling hysteresis of (a) butane (b) hexane and (c) octane microjets.*

To estimate heat flux near the critical power (critical heat flux, CHF), a finite difference heat transfer simulation was performed considering temperature dependent thermal conductivity and electrical resistivity. From the cantilever operation without jet impingement, the cantilever-air thermal conductance was extracted. Then, the extracted cantilever-air conductance was used for the differential nodes that were not influenced by the microjet impingement and the cantilever-microjet conductance was used as a fitting parameter. The simulation calculated the convective heat transfer from the cantilever

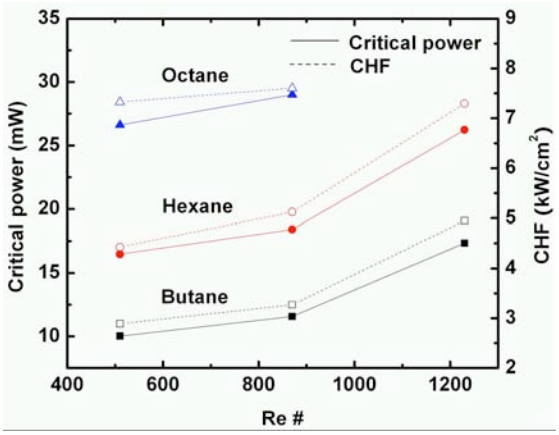

Figure III.7: *Measured critical power and simulated CHF as a function of Re for three hydrocarbon microjets.*

heater to the microjets and heat fluxes were obtained based on the surface area of the heater. Fig. III.7 compares the experimented critical power and simulated CHF for butane, hexane, and octane at different Re numbers. Both the critical power and CHF increase with Re and octane microjets have the highest critical power and CHF at a given Re. Due to these similar trends, CHF can be estimated directly from the measured critical power later on.

III.2 Nanojet Metrology using Piezoresistive Cantilevers

Initially, measurements were performed with commercial piezoresistive cantilevers. In later project stages, dedicated piezoresistive cantilevers were fabricated and used for microjet metrology.

Figure III.8(a) shows the measured cantilever deflection as a commercial piezoresistive cantilever is traversed through gaseous nitrogen jets generated from a 1 μm diameter microfabricated nozzle. In contrast to the liquid jet, the gaseous jet shows almost symmetric deflection curves having a maximum deflection when the cantilever is aligned to the center of the nozzle. As an example, Figure III.8(b) shows a Gaussian-like deflection curve when the driving pressure is 9.65 MPa (see cross-section AA´ in Figure III.8(a)). Figure III.8(c) shows the linear relationship between the cantilever maximum deflection and the driving pressure using gaseous nitrogen jets from the 1 μm diameter nozzle. Once the driving pressure is fixed, the cantilever maximum deflection can be estimated.

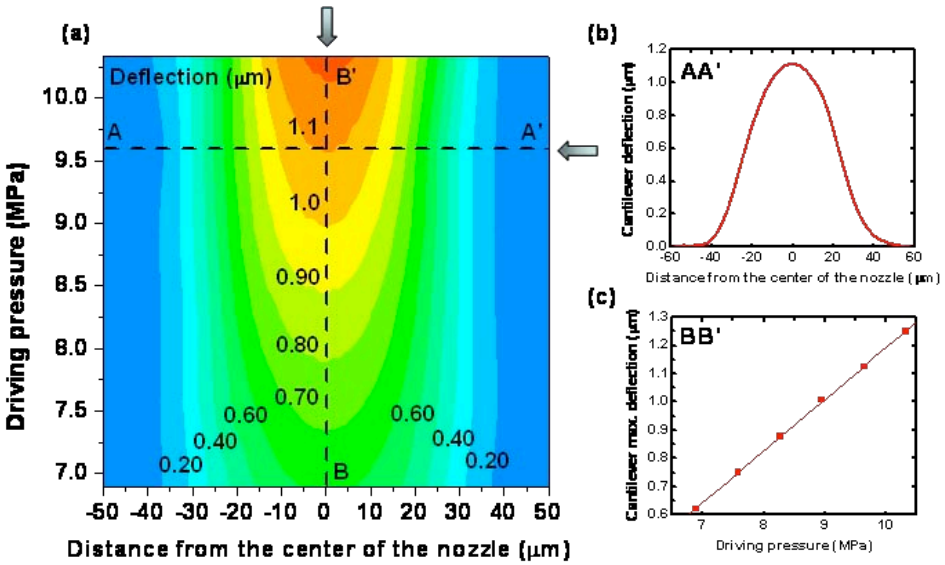

Figure III.8: (a) Contour plot of deflection of the piezoresistive cantilever as the cantilever is traversed through gaseous nitrogen jets (b) A Gaussian-like deflection curve when the driving pressure is 9.65 MPa (c) Linear relationship between cantilever maximum deflection and driving pressure. Gaseous nitrogen jets are generated from an 1 μm diameter nozzle with 27 μm separation between the cantilever and the nozzle.

The newly designed and fabricated piezoresistive cantilever (see Fig. III.1b) was configured in a Wheatstone bridge that was interfaced with a real-time spectrum analyzer

(Tektronix, RSA3303A). The piezoresistive cantilever was aligned to and impinged upon by a hexane microjet and the initial vertical position was referenced to the nozzle exit using the auxiliary laser optical system. The lateral position of the jet impingement was 150 μm from the cantilever base and this position was fixed during a measurement. While the gap distance between the cantilever and the nozzle exit was varied, the spectrum analyzer output was recorded and analyzed. Fig. III.9 shows the power spectrum density (PSD) from the spectrum analyzer and corresponding Lorentzian curve fit at three different gap distances – 1.000 mm, 1.037mm, and 1.073mm, respectively where the hexane jet velocity is 27 m/s. When the gap distance is less than 1.037 mm, the fitted Lorentzian peak becomes less pronounced or nearly flat. However, when the gap distance is greater than 1.037 mm, the peak becomes intense enough to be observed. Therefore, there exist two different flow regimes. When the piezoresistive microcantilever is located close to the nozzle exit, static deflection is dominant and the microcantilever motion will be highly damped such that no observable peak exists in the frequency domain of interest. However, when the cantilever is impinged on by discrete droplets, the PSD shows a distinctive peak in the given frequency band. Therefore, the breakup distance of the microjet can be determined by applying an appropriate PSD threshold.

Fig. III.10(a) shows contour and projection plots of the PSD in a wide range of gap distances. The peak disappears around 1.03 mm, which is the breakup distance. Fig. III.10(b) shows the peak frequency, width (FWHM: Full width at half maximum), and quality factor as functions of the gap distance. The peak frequency changes periodically between 16 and 25 kHz in the direction of the jet flow. The shape of the peak characterized by the peak intensity and the quality factor also changes with the gap distance. The peak intensity oscillates somewhat but shows a slight overall increase with the gap distance. The quality factor exhibits strong dependence on the gap distance thus breakup. The quality factor becomes maximized around at 1.073 mm then decreases drastically and becomes insensitive to further gap distance change when the gap distance is greater than 1.073 mm. Therefore, both the peak intensity and the quality factor can be a measure of the microjet breakup.

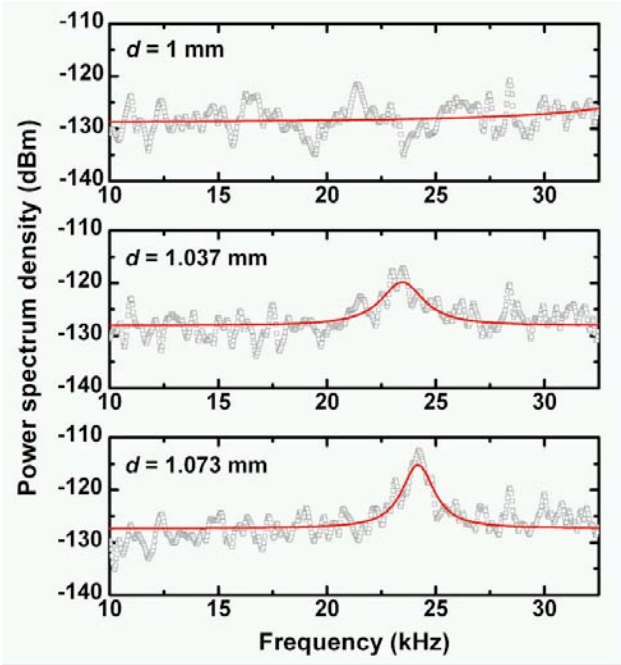

Figure III.9: *Power spectrum densities from a real-time spectrum analyzer and corresponding Lorentzian curve fits at three different gap distances 1.000 mm, 1.037mm and 1.073 mm, respectively. The hexane jet velocity is 27 m/sec and the jet diameter is 10 μm.*

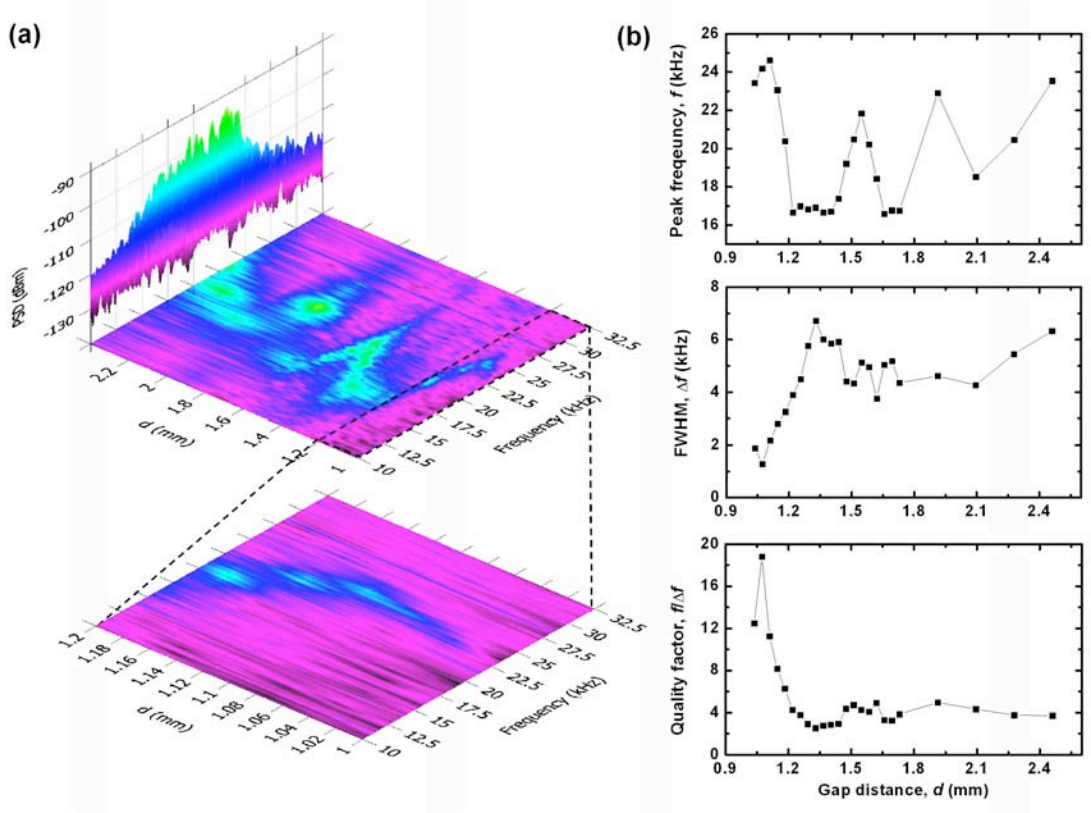

Figure III.10: *Contour and projection plots showing characteristic behaviors in the frequency domain before and after jet breaks up into droplets. (b) Peak frequency, FWHM, and quality factor as a function of gap distance.*

III.3 Development of Piezoresistive Cantilevers using Stress-Concentrators

Piezoresistive cantilevers with their integrated read-out are a prominent choice for characterization of micro- and nano-jets. The force sensitivity (S) of a piezoresistive cantilever can be divided into 3 partial sensitivity terms associated to the transduction of a) force F to deflection z (S_1), b) deflection to stress σ (S_2), and c) stress to relative resistance change dR/R (S_3)

$$S = \frac{dz}{dF} \times \frac{d\sigma}{dz} \times \frac{dR/R}{d\sigma} = S_1 \times S_2 \times S_3$$

S_3 only depends on the piezoresistive coefficients. For a simple cantilever beam, the maximum longitudinal stress occurs on the surface and its magnitude increases toward the clamped-edge. The maximum longitudinal stress increases by reducing the radius of bending curvature; i.e. for a given force, by decreasing the beam stiffness [1]. In piezoresistive cantilevers, the conventional method to improve the force sensitivity is to

[1] R. R. Archer, N. H. Cook, S. H. Crandall, N. C. Dahl, F. A. McClintock, E. Rabinowicz, and G. S. Reichenbach, *An introduction to the mechanics of solids*. New York: McGraw-Hill, 1959.

reduce the stiffness by making the beams thinner, i.e. increasing S_1 [2]; however, despite of all its effectiveness, the resulting reduction of resonance frequency overshadows the sensor performance. Moreover, as mentioned before, the decrease of the beam stiffness results in fragile devices that can be damaged during harsh-environment testing, such as the interaction with the jet flow in this project. Finally, the less stiffness, the larger is the cantilever deflection for a given force; hereupon the deflection is comparable to the cantilever length, the cantilever will exhibit a nonlinear bending, thus a nonlinear output signal. In piezoresistive cantilevers, instead of increasing the stress in the entire beam volume, it is also possible to concentrate the strain energy in fractions of the beam, where the sensing elements are located; this way, the force sensitivity can be increased without reducing the overall thickness of the beam.

In this project part, cantilevers based on a stress-concentration principle have been designed, fabricated and tested (see Fig. III.11). In the adopted design, stress-concentrating (SC) beams and nanowires, hereafter generally referred to as SC elements, are suspended over a notch etched into the cantilever and, thus, the sensitivity S_2 is increased without sacrificing S_1.

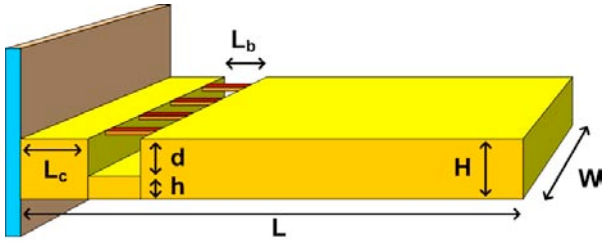

Figure III.11: *Simplified schematic of an SC cantilever with symbols for the main dimensions.*

The advantage of the stress-concentration concept is shown in Fig. III.12, which compares the simulated cantilever stiffness and the average longitudinal stress acting on the SC element as a function of the notch depth d. In the corresponding finite element simulations, performed using COMSOL, the cantilever length L, width W, and thickness H are 350, 70, and 20 µm, respectively. The SC elements are 10 µm long, 2.5 µm wide, 0.5 µm thick, and located L_c = 5 µm from the clamped edge of the cantilever. The spacing between adjacent SC elements is 2.5 µm. The cantilevers are deflected by applying a constant point force, F = 1 mN, on their tip. The results are normalized with the corresponding values for a solid cantilever of the same total thickness, i.e. 20 µm, having no notch. For both cantilever types, the maximum longitudinal stress is monitored at 10 µm distance

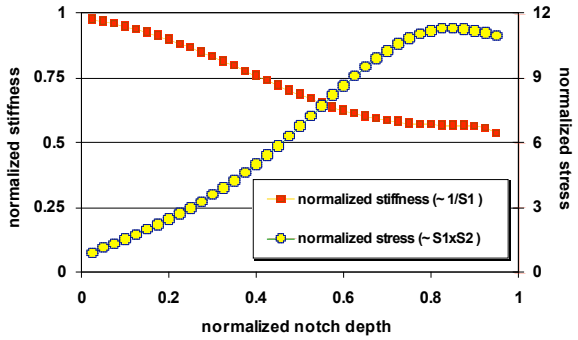

Figure III.12: *Normalized simulated cantilever stiffness and average stress acting on SC elements (for 1mN tip force) as a function of normalized notch depth d/H. The stress and stiffness are normalized with respect to the values of a solid cantilever (d/H = 0).*

[2] J. A. Harley and T. W. Kenny, "High-sensitivity piezoresistive cantilevers under 1000 angstrom thick," *Applied Physics Letters*, vol. 75, pp. 289-291, 1999.

from the clamped edge, which corresponds to the location of the SC elements center-point, i.e. the point where the average stress is acting on the SC elements.

Based on the simulation results, the induced stress in the SC cantilever is considerably higher than that in the solid cantilever as long as *h*, the remaining thickness under the notch, is not smaller than the thickness of the SC elements. This gain comes at the price of only up to 50% decrease in stiffness. This advantage is also shown in Fig. III.13, where the stress and the stiffness of the same SC cantilever are compared to a solid conventional cantilever having the same length and width as in the previous case, but a thickness equal to *h*, i.e. the remaining thickness under the notch in the SC cantilever. As shown in Fig. III.13, as long as *h* is larger than 5 µm, the SC cantilever experiences a higher stress than the solid cantilever; and while the stress is smaller in the SC cantilevers for h < 5 µm, they continue to exhibit their significant superiority in terms of stiffness.

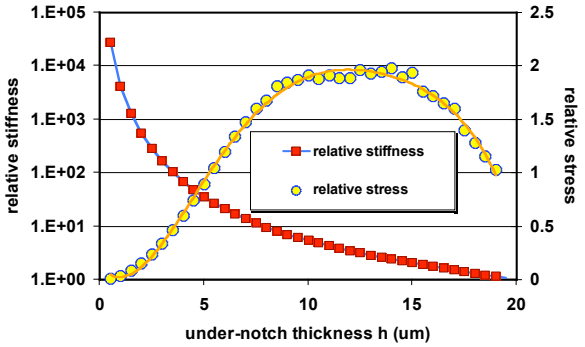

Figure III.13: *Ratio of the simulated stiffness and stress in a 20 µm-thick SC cantilever to the corresponding values in a solid cantilever with the thickness of h (see Fig. 1) as a function of the remaining thickness under the notch h.*

Devices have been fabricated on epitaxially-grown (100) silicon wafers. The 17 µm device layer is n-doped and the handle layer is p-doped. The piezoresistive areas are defined by boron diffusion. The embedded stress-concentrating beams and nanowires are fabricated according to the process flow of Fig. III.11. In this process, which requires only one UV lithography mask, the beams and nanowires can be repeatedly batch-fabricated (unlike a serial processing of nanowires using E-beam writing technique). The fabrication of the SC elements starts with a thermal oxidation of the wafer surface, followed by pattering parallel windows on the oxide layer in <110> direction. Then, using an inductively couple plasma, the oxide layer and the underlying silicon are etched to form shallow trenches (<1.2 µm) into the device layer.

Next, another thermal oxide layer is grown to conformally cover the sidewalls and bottoms of the etched trenches. The purpose of growing the latter oxide layer is to protect the silicon bars in-between the trenches during the upcoming etching steps. The SC beams and nanowires are constructed within these bars; hence, the shape of the bar, i.e. the shape of the trenches, determines the final dimensions of the beams and nanowires. In the next step, the oxide layer is removed from the trench bottoms using reactive ion etching, and the trenches are further etched, while no significant decrease is observed in the sidewall oxide thickness. To release the SC elements, the wafer front-surface is immersed in a 6-molar KOH solution at 30 ºC for approximately 60 minutes. The etching time depends on the spacing between adjacent trenches, and the targeted shape of the SC elements, i.e. either beams or nanowires. To successfully release the doubly-clamped nanowires, the length of adjacent trenches (see Fig. III.14(a)) should not be equal.

Because of the anisotropic etching, the notch floor is not even. For the reported devices here, the average notch depth is 9.3 µm. To release the cantilevers, the wafer is anisotropically etched from the backside in KOH solution. The final geometry of the cantilever is defined by frontside dry etching. The fabricated cantilevers are 346 µm long, 70 µm wide, and 17 µm thick. Due to the deposition of an extra passivation oxide layer, the released beams and wires are covered with a 0.8 µm thick oxide layer. Also, due to wafer thickness variations, the clamped-edge of the cantilevers does not coincide with the edge of the etched cavity; instead, the cantilever is supported by an 18 µm wide rim of the same thickness. Fig. III.15 shows an SEM micrograph of a fabricated device, with the SC elements, covered by the clad oxide, suspended over the notch.

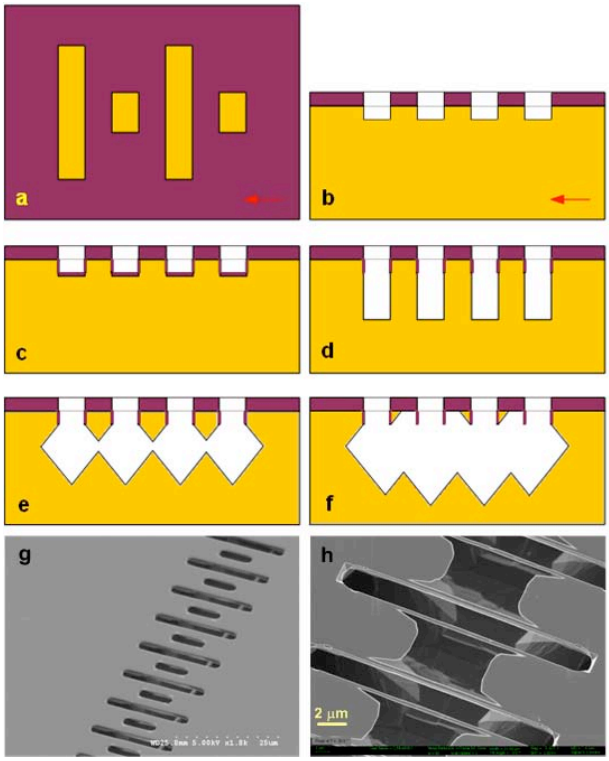

Figure III.14: *Fabrication process flow for SC elements:* ***a)*** *top-view of mask layout for trench etching; the arrow indicates the [110] direction; Cross-sections after* ***b)*** *etching shallow trenches,* ***c)*** *covering sidewalls and bottom of the trenches with thermal oxide;* ***d)*** *deepening the trenches using deep reactive ion etching* ***e)*** *releasing the beams by KOH etching,* ***f)*** *additional anisotropic etching, and releasing nanowires inside the clad oxide layer (highlighted with the circle);* ***g&h)*** *SEM micrographs of released SC beams and nanowires, respectively, after removing the clad oxide in HF.*

Using a Berkovich tip with a Hysitron TriboIndenter®, different preset forces were exerted on the free-end of the cantilever and the resulting deflections were recorded with sub-nanometer precision. Meanwhile, the resistance change in the piezoresistors was measured by a Keithley 2400 Sourcemeter®. The dissipated power in the piezoresistors was set at 20 ± 5 µW.

Fig. III.16 compares the force sensitivity and the spring constant of three SC cantilevers to a solid cantilever. Two of the SC cantilevers have nanowires, and the third one has SC beams as the stress-concentrating elements. The cantilever with thinner nanowires is associated with a higher resistance. Fig. III.16 shows that for the thinner SC elements the sensitivity is higher, while the stiffness is slightly smaller. It should be noted that since only a fraction of the measured resistance is aligned with the longitudinal stress, in case of the thicker SC elements a larger fraction of the overall resistance of the piezoresistor is not affected by the stress, and thus the sensitivity is reduced compared to the device with thinner SC elements. This issue is an additional reason for the large difference between the sensitivity of cantilever with nanowires and the one with beams. The specifications of

the cantilevers are summarized in Table III.I. The force sensitivity of the SC cantilever with thinner nanowires (117 kΩ) is 8.0 times larger than that of solid cantilever, which is consistent with the simulation results in Fig. III.9 for d/H = 0.55, and 5.7 times larger than the sensitivity in the SC cantilever with micrometer-sized beams. The reduction in stiffness is less than what has been predicted by the simulation. This issue can be attributed to the presence of the cavity rim, which results in a decrease of the solid cantilever's stiffness.

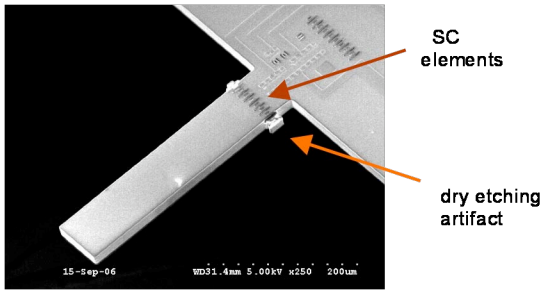

Figure III.15: *SEM micrograph of a fabricated cantilever; the stress-concentrating elements (covered by the clad oxide) are suspended over the notch, 25 μm from the clamped edge.*

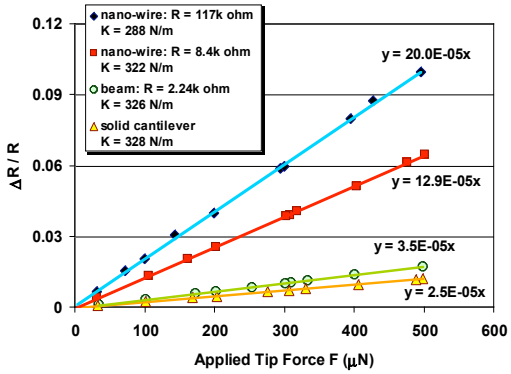

Figure III.16: *Relative resistance change as a function of the applied tip force for a solid cantilever (triangles), cantilevers with stress-concentrating Si-nanowires with resistance R=8.4kΩ (squares) and R=117kΩ (diamonds), and a cantilever with stress-concentrating beam (circles).*

SC element	*R (kΩ)*	*K (N/m)*	*Deflection sensitivity (nm^{-1})*	*Force sensitivity - static (mN^{-1})*
Nanowire	**117**	**288**	**$56.9\ 10^{-6}$**	**$20.0\ 10^{-5}$**
Nanowire	**8.4**	**322**	**$40.8\ 10^{-6}$**	**$12.9\ 10^{-5}$**
Beam	**2.24**	**326**	**$11.6\ 10^{-6}$**	**$3.5\ 10^{-5}$**
None (solid)	**1.55**	**328**	**$8.0\ 10^{-6}$**	**$2.5\ 10^{-5}$**

Table III.I: *Characteristics of cantilevers with different SC elements.*

IV. Molecular Dynamics Simulations

IV.1 Nanojet and Nanobridge Breakup Processes

Breakup (or pinch-off) processes of liquid structures (e.g., jets and junctions) attract lasting interest in recent years [1] and is motivated by both theoretical inquiry and technological applications. The pinch-off process is the final stage of breakup of a liquid structure, resulting in the formation of droplets, and as such it is of relevance to various applications such as ink-jet printing [2], fuel injection [3] and spraying [4], drug delivery and encapsulation. The pinching process of one liquid structure injected into or embedded in an ambient fluid environment is of great importance for mixing process, as well as formation of core-shell structures. Furthermore, most of the experiments performed under this project are performed for miniaturized fluid structures in ambient conditions (not in vacuum), consequently fundamental understanding of the behavior under such conditions is of paramount importance.

From a fundamental theoretical perspective interest is focused on the development of the singularity that occurs when a liquid structure approaches the breaking point, and the self-similarity, scaling and universality phenomena near the singularity. Investigations of pinching processes in macroscopic systems commonly utilize the Navier-Stokes equations, both with and without ambient environments [1,2,5,6,7], leading to the derivation of scaling laws pertaining to the behavior near pinch-off. While such investigations are most valuable, it is also clear that these capillary-driven processes, ultimately involve such small length scales where the fragmenting fluid cannot be regarded any further as a continuum and where thermal fluctuations, and size-dependent effects, must be considered (and perhaps dominate the processes). The relevant length scale can be estimated as $l_T = \left(k_B T / \gamma\right)^{1/2}$ [8], which at room temperature is in the nanometer range for almost all fluids. Previous results [9] showed that, in the nanometer scale, the typical pinching time of liquid filaments is of the order of nanosecond. While current technical difficulties make direct experiments probing on such small spatio-temporal scales, the development of the computational techniques open new avenues for simulation and discovery in this area.

As discussed in [9] and [10], in the nanometer scale, deterministic methods are invalid to describe the pinching processes and stochastic methods have to be utilized. Hence, each individual liquid bridge system may experience different perturbations (that is, a different realization of the noise, or fluctuation, process), and thus it may evolve along a different trajectory. When circumstances are such that the intrinsic stochastic fluctuations (as well as external stochastic influences) are of comparable importance as the forces that govern the deterministic trajectories of the system, one may expect to observe a much richer spectrum of behavior in the stochastic systems than that characteristic of the deterministic regime (that is, certain events that have a small probability of occurrence in the deterministic domain, may acquire a high occurrence probability in the stochastic regime).

Using a newly developed atomistic molecular dynamics (MD) simulation method, we demonstrated the behavior of nanometer-scale liquid jets and bridges, both with and without ambient gas environments. We have found that the pinch-off processes exhibit different has different characteristics depending on whether the gas nanostructure evolves in vacuum or in an ambient gaseous (or liquid) environment. The pinching processes in vacuum (free surface) exhibit a power-law scaling of the time dependence and the similarity profiles near the pinch-off singularity; and the simulated time dependence of the minimum neck radii is in good agreement with the theoretical prediction [10] obtained through analysis of the stochastic lubrication equations (SLE) derived in ref. [9]. We also show that the presence of an ambient gas (nitrogen in our simulations with a propane liquid nano-bridge or nanojet) modifies the geometric profiles of the pinching processes. Most importantly, increasing density of the surrounding gaseous nitrogen makes *the symmetric similarity profile* (discovered for nano liquid structures in vacuum, see ref. 9, see Figure IV.1) becomes less dominated, with increasing probability of occurrence of the *asymmetric profiles* (long-thread, or thread-cone, profile, see Figure IV.2), which is characteristic of the breakup processes of macroscopic fluid structures.

For axisymmetric liquid bridges in vacuum the breakup profiles are close to the symmetric in shape. We anticipate that the breakup process will exhibit self-similarity when the bridge approaches the pinching point. The general forms for the shape and velocity of a symmetric pinching profile of a bridge can be described as,

$$h(z,t) = (t_0 - t)^{\alpha} f\left(\frac{z}{(t_0 - t)^{\beta}}\right), \tag{IV.1}$$

$$v(z,t) = (t_0 - t)^{\gamma} g\left(\frac{z}{(t_0 - t)^{\beta}}\right), \tag{IV.2}$$

where, h (z, t) is the time dependence of the radius of the bridge along the azimuthal axis, z, and v (z, t) is the time dependence of the velocities at different points along the z axis. t_0 is the pinch-off time; f and g are different universal profiles of h and v expressed in terms of the corresponding similarity coordinates, and α, β and γ are different similarity indexes. If we set the origin of the z axis at the center of the bridge, for symmetric profile, f is an even function of z, and v is an odd function of z, which implies that f reaches a fixed minimum value at z=0, and that g has a fixed maximum value at some points on the z axis. Hence, we obtain that,

$$h_{min} \sim (t_0 - t)^{\alpha}, \tag{IV.3}$$

$$v_{max} \sim (t_0 - t)^{\gamma}. \tag{IV.4}$$

To measure α, we repeat the simulations several times. From the time dependence of h_{min} plotted vs $(t_0 - t)$ in log-log coordinates, an average value of α=0.40 is determined. The result is within 5% of the theoretical prediction by Eggers [10], which is 0.418. The measured value is much less than 1, which means that the pinching processes of the

liquid nano-bridges have a power law time dependence of the minimum neck radius, instead of the linear time dependence in macroscopic pinching processes. The difference verifies that in the nanometer scale, the surface tension is not the most important driving force for the pinching process of the liquid bridge. Instead, the fluctuations appear to provide the dominant driving force. When the same procedure is followed in simulations of the breakup process of nanobridges in a gaseous environment, we find often (depending on the pressure of the ambient gas) a linear dependence of h_{min} on $(t_0 - t)$, i.e. α=1 in Eq. (3), coinciding with the prediction at macroscopic length scales. A similar trend is found for the exponent of the velocity time dependence near pinch-off. These results correlate with the results for the shape profiles shown in Figs. 1 and 2.

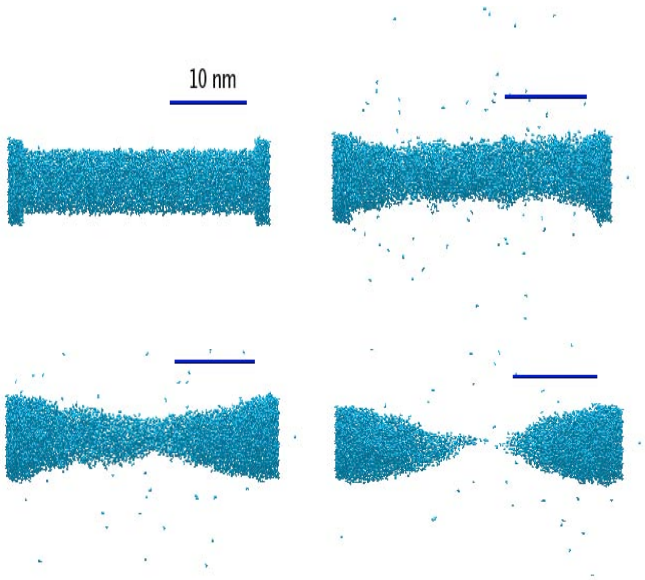

Figure IV.1: *Molecular dynamics simulation of a nano-bridge junction breakup process in vacuum. A typical pinching processes of free surface liquid bridge at t = 0, 200, 400 and 547 ps, exhibiting two-cone symmetric profile. The diameter of the bridge is 6 nm and the length of the bridge is 30 nm. There are two short cylindrical supporting pads at both ends of the bridge (see upper left). The diameter of the covers is 4 nm and the height of them is 2 nm. Inside the covers the propane molecules are fixed.*

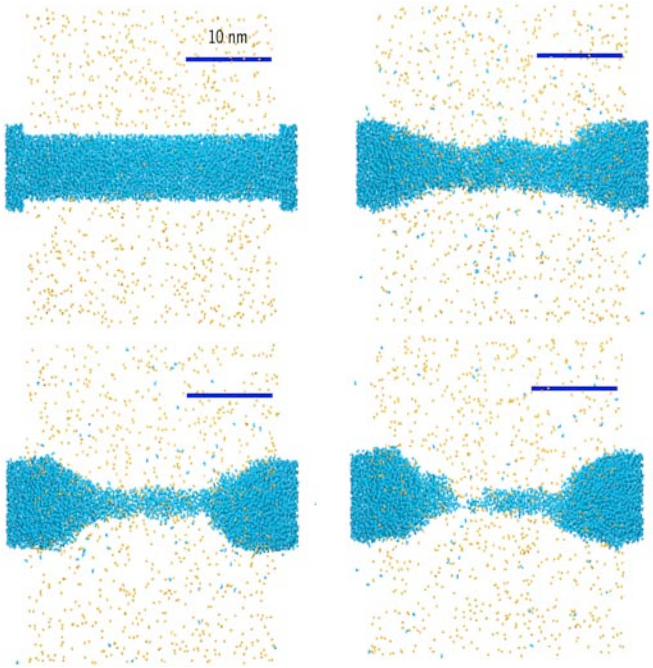

Figure IV.2: *Molecular dynamics simulation of the pinching process of a propane nano liquid bridge with ambient nitrogen gas environment at t=0, 400, 760, 840 ps., showing an asymmetric (long-thread) profile. The diameter of the bridge is 6 nm and the length of the bridge is 30 nm. The density of the gas is 6.0 kg/m^3.*

References

1. J. Eggers, Rev. Mod. Phys. 69, 865 (1997).
2. J. R. Lister and H. A. Stone, Phys. Fluids. 10, 2785 (1998).
3. K. Kuo, Ed., Recent Advances in Spray Combustion: Spray Atomization and Drop Burning Phenomena (American Institute of Aeronautics and Astronautics, Reston, VA, 1996), vols. 1 and 2.
    A. L. Yarin, Free Liquid Jets and Films: Hydrodynamics and Rheology (Longman, Essex, UK, 1993).
4. J. Eggers, Phys. Rev. Lett. 71, 3458 (1993).
5. J. Eggers. Phys. Fluids. 7, 941 (1995).
6. R. F. Day, E. J. Hinch and J. R. Lister, Phys. Rev. Lett. 80, 704 (1998).
7. X. D. Shi, M. P. Brenner, and S. R. Nagel, Science 265, 157 (1994).
8. M. Mosler and U. Landman, Science 289, 1165 (2000).
9. J. Eggers, Phys. Rev. Lett. 89, 084502 (2002).

IV.2 Virtual Nanojet Nozzle

Aiming at the development of methods for the generation of nanojets that alleviate the severe requirements prescribed by our original schemes (pertaining to geometric nozzle design and high injection back-pressures), we have reported recently on molecular dynamics simulations where a "virtual nozzle" effect was discovered, generated via the flow of a fluid (propane) through a heated cylindrical injector tube (see Fig. IV.3). In effect we have shown that by heating the tube walls one can raise the temperature of the liquid in contact with the walls and consequently create a flowing liquid structure that has a temperature gradient between the walls and the central core of the liquid in the cylinder. The temperature profile varies not only radially but also along the propagation axis (z), and it is portrayed in the density profile of the liquid which exhibits (inside the injector, that is, prior to exit) the shape of a converging nozzle – hence the name "virtual nozzle" (see Figs. IV.4 and IV.5). Since the emission of the jet from the tube is accompanied by massive molecular evaporative cooling from the surface of the jet (typically over a distance from the exit point of about 50nm), the resulting nanojet is of low temperature and it is of a reduced diameter compared to that of the injector tube diameter. This achieves one of our goals – namely, the employment of larger diameter injectors for the creation of nanojets. Furthermore, the pressure required to create the nanojet is smaller then in our original method because of the larger radius of the tube used in the new technique, as well as the reduced friction between the hot liquid and the heated walls.

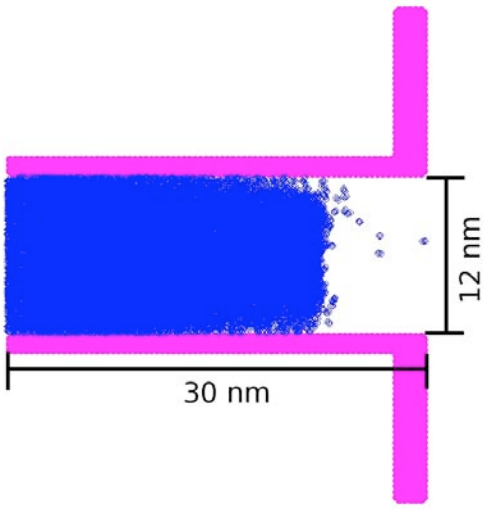

Figure IV.3: *Cross-sectional view of the injection tube, consisting of a cylinder with a uniform diameter of 12 nm and a length of 30 nm. Liquid propane enters the nozzle from the left end with a velocity of 250 nm/ns and with a temperature of 150 K. The pressure at the left end is 220 MPa while the pressure at the right opening is near 0 MPa. The temperature of the internal wall of the nozzle is kept at 500 K.*

The principles of the heated-injector scheme are shown in Figs. IV.3-5. The length of the heated part of the nozzle shown in Fig. IV.3 is 30 nm (the preceding non-heated part of the nozzle is not shown) and its diameter is 12 nm. The temperature of the nozzle is 500 K. Propane enters the heated part of the nozzle (the left end in Fig. IV.3), with a local pressure of 220 MPa and a velocity of 250 nm/ns. At the right opening of the nozzle, the pressure of the propane vanishes.

The virtual nozzle effect, as obtained from our MD simulations, is illustrated in Figs. IV.4 and IV.5 for the temperature and density profiles, respectively. These figures show formation of a fluid density profile (inside the heated tube) shaped as a convergent nozzle (see Fig. IV.5). Our objective now is to develop a continuum hydrodynamic model that

would enable convenient explorations of virtual nozzle design. The first step toward the development of such model is a description of the liquid whose properties vary in a large range as the pressure inside the injector tube decreases from 220 MPa to almost 0 MPa and the liquid is heated from 150 K (in the reservoir) to 500 K (close to the internal wall of the nozzle). However, a proper description can be obtained with assistance from our MD simulations.

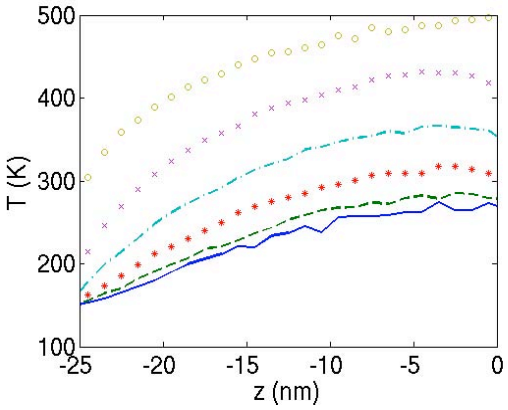

Figure IV.4: *Temperature field inside the nozzle obtained though an MD simulation. The (blue) solid curve corresponds to the central region with a radius of 1 nm, the (green) dashed curve is for a ring extending from 1 to 2 nm, the (red) star curve is for the 2-3nm ring, the (sky blue) dash-dot curve is for the 3-4 nm ring, the (purple) cross curve is for 4-5nm and the (yellow) hollow-circle curve is for the 5-6 nm ring. Note that the temperature of the center part is much lower than the outer part.*

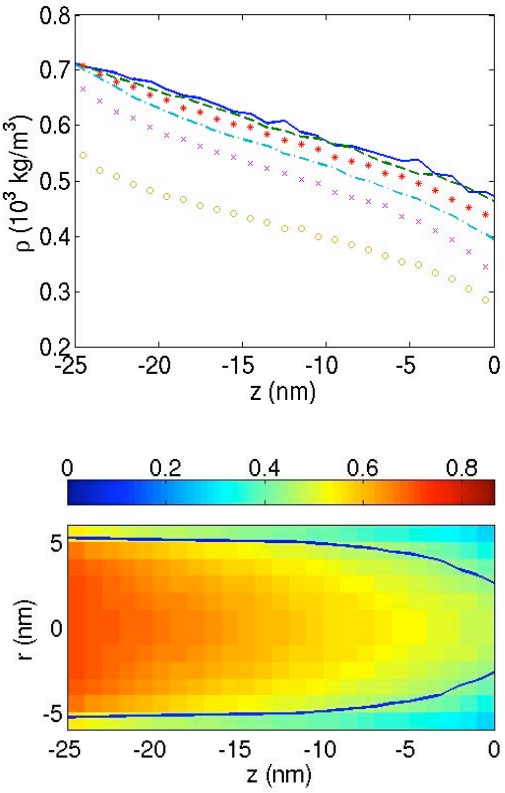

Figure IV.5: *(a) Density field inside the nozzle obtained though MD simulation. The meaning of the symbols is the same as that in Fig. IV.2. (b) Color-coded density distribution inside the hot nozzle obtained through the MD simulation. The unit of the density is 10^3 kg/m^3. The blue solid curves are the contour lines associated with a density of 0.4×10^3 kg/m^3. This line delineates the shape of the virtual convergent nozzle. The shape of the virtual nozzle is closed to that in (a).*

Generally, the flow inside the nozzle is governed by the Navier-Stokes equations [1]. With the axial symmetry of the flow, the equations are expressed in the cylindrical coordinates as [1,2],

$$\frac{\partial u_r}{\partial t} + u_r \frac{\partial u_r}{\partial r} + u_z \frac{\partial u_r}{\partial z} = -\frac{1}{\rho}\frac{\partial p}{\partial r} + \nu\left\{\frac{\partial}{\partial r}\left[\frac{1}{r}\frac{\partial}{\partial r}(r u_r)\right] + \frac{\partial^2 u_r}{\partial z^2}\right\}, \quad \text{(IV.5)}$$

and

$$\frac{\partial u_z}{\partial t} + u_r \frac{\partial u_z}{\partial r} + u_z \frac{\partial u_z}{\partial z} = -\frac{1}{\rho}\frac{\partial p}{\partial z} + \nu\left[\frac{1}{r}\frac{\partial}{\partial r}\left(r\frac{\partial u_z}{\partial r}\right) + \frac{\partial^2 u_z}{\partial z^2}\right], \quad \text{(IV.6)}$$

where, u_r , u_z are the r, z components of the velocity field respectively; ρ is the density of the flow; p is the local pressure; and ν is the kinematical viscosity of the flow and is defined as the ratio of the viscosity μ and the density ρ. Usually, ν is a function of the local pressure p and the local temperature T of the propane flow; however, to simplify the problem, a constant effective $\nu = 2.8\times10^{-7}$ nm^2/ns is used in the model. From the MD simulations, we found that (as shown in Fig. IV.6) the pressure of propane inside the nozzle is well described by a linear function of z, i.e., $\partial p/\partial r$ is 0 and $\partial p/\partial z$ is a constant. Note that these two conditions pertaining to the pressure are used as known conditions. It is one of the major approximations of our continuous model and is different from the usual computational fluid dynamics (CFD) calculations [3,4], where the pressure field p(z, r, t) is a variable of the equation of motion.

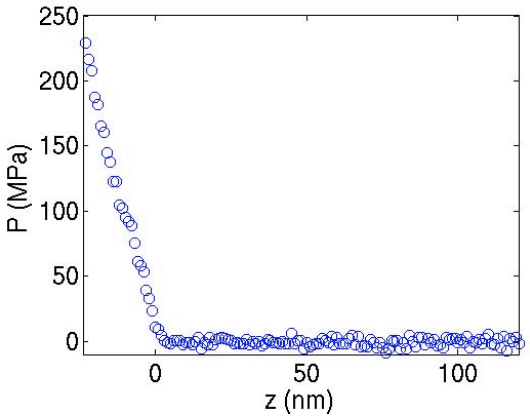

Figure IV.6: *The pressure distribution in the propane liquid as a function of z (the flow direction). The data is obtained from an MD simulation of nanojet formation. The nozzle occupies the region with z < 0. The pressure change inside the nozzle can be well described by a linear function of z.*

In our model, the energy change of the flow is depicted by the variation of the temperature field instead of the full energy conservation equations. The equation for the change of temperature field, denoted as T, is

$$\frac{\partial T}{\partial t} + u_r \frac{\partial T}{\partial r} + u_z \frac{\partial T}{\partial z} = \kappa\left[\frac{1}{r}\frac{\partial}{\partial r}\left(r\frac{\partial T}{\partial r}\right) + \frac{\partial^2 T}{\partial z^2}\right], \quad \text{(IV.7)}$$

where κ is the thermometric conductivity of the flow. From the MD simulation, we know that the temperature gradient of the propane flow is about 50 K/nm from the internal wall to the center of the flow. Such a large temperature gradient implies that the energy change in the flow is mainly caused by heat transfer. Moreover, since the flow is confined in the nozzle, the volume change is small and thus contributes a small part to the

energy change of the flow. These suggest that the change of the temperature field of the flow is a reasonable approximation to the total energy change. We also notice that the model can be further simplified by adopting a constant thermometric conductivity of $\kappa = 1.01\times10^2$ nm^2/ns.

To proceed we need to formulate an equation of state of the material (in our case, propane) inside the nozzle. In some parts of the flow, the propane liquid experiences such a high pressure (over 200 MPa) that experimental data are difficult to obtain in this range. It is convenient for us to get an approximate equation of state of propane from the MD simulation data. For the relevant pressure and temperature range, the following simple equation of state provides an adequate description of propane. As a function of density ρ, pressure p, and temperature T, the equation of state may be written as

$$\rho(p,T)=\left[\rho_0-\alpha\left(1-\frac{p}{p_0}\right)\right]\left[1-\beta(T-T_0)\right], \qquad \text{(IV.8)}$$

where, $\rho_0(p_0,T_0)$ is a reference point in the phase space for the linear equation of state, and α, β are pressure, temperature coefficients respectively. In our model the reference point is p_0 = 220 MPa, T_0 = 150 K, and $\rho_0 = 0.72\times10^3$ kg/m^3. The coefficients are $\alpha=0.19\times10^3$ kg/m^3 and $\beta=1.2\times10^{-3}$ K^{-1}.

Since we have assume the pressure variation to be known *a priori* (found from the MD simulation to vary linearly with distance from the entry point, see Fig. IV.6), Eqs. (IV.5-8) form a complete set of equations for variables u_z, u_r, T and ρ. The continuity equation,

$$\frac{\partial\rho}{\partial t}+\frac{1}{r}\frac{\partial}{\partial r}(r\rho u_r)+\frac{\partial}{\partial z}(\rho u_z)=0\,, \qquad \text{(IV.9)}$$

is used as a consistency check.

In addition to the aforementioned boundary conditions, to make the model a well-posed problem, we need also to know the velocity of the moves at the internal wall of the nozzle. Our MD simulations revealed that the wall is entirely non-sticking after a short transient distance. The velocity of the liquid at the wall decreases from 250 nm/ns to 150 nm/ns over a transient distance and subsequently it remains constant. In our model, we simply neglect the short transient distance and take the velocity of the flow on the internal walls of the nozzle to have the value 150 nm/ns.

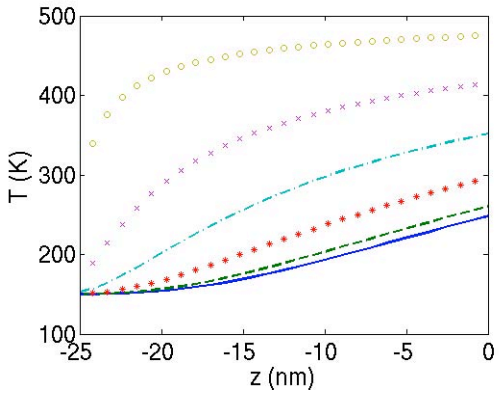

Figure IV.7: *Temperature field inside the nozzle obtained though the continuum hydrodynamic model. The (blue) solid curve corresponds to the central region with a radius of 1 nm, the (green) dashed curve is for a ring extending from 1 to 2 nm, the (red) star curve is for the 2-3nm ring, the (sky blue) dash-dot curve is for the 3-4 nm ring, the (purple) cross curve is for 4-5nm and the (yellow) hollow-circle curve is for the 5-6 nm ring. Note that the temperature of the center part is much lower than the outer part.*

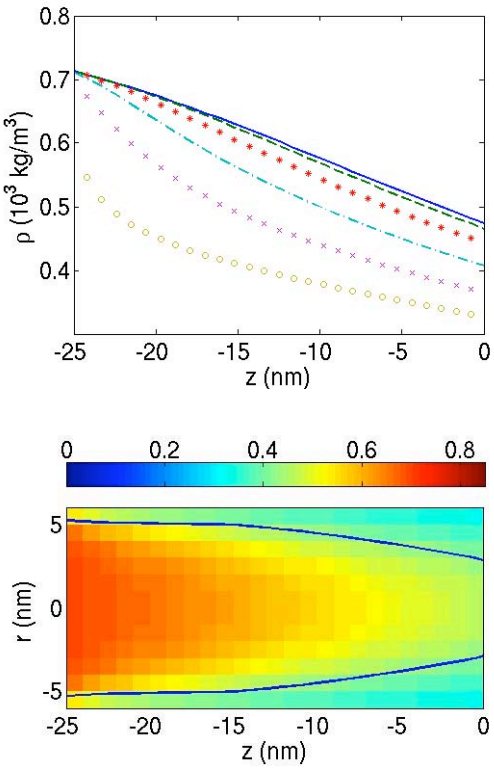

Figure IV.8: *(a) Density field inside the nozzle obtained though the hydrodynamic continuum model. The meaning of the symbols and colors is as given in Fig. IV.5. (b) Color-coded density distribution inside the hot nozzle obtained through the continuum hydrodynamic model. The unit of the density is 10^3 kg/m^3. The blue solid curves are the contour lines corresponding to a density of 0.4×10^3 kg/m^3, delineating explicitly the shape of the virtual convergent nozzle.*

In principle, as indicated by the MD simulation, the flow in the nozzle achieves a stationary state sometime after entering the heated part of the nozzle. In our present hydrodynamic model we do not consider this relaxation time period, assuming stationary state flow from the start. This is not expected to influence our conclusions about the formation of the virtual nozzle effect toward the exit.

The model is solved using a finite difference numerical method [3,4] on a regular 30×12 grid. The entire volume in the nozzle is divided into 30 grid cells along the axial direction, and 12 grid cells along the radial direction. The Maccormack's technique [3,4] is employed with a small time step of 1.0 fs. The numerical solutions for the axial and radial velocities (u_z and u_r), temperature, T, and density, ρ, are obtained; the latter two quantities are shown in Figs. IV.7 (T) and IV.8 (ρ). Our results show that the quantities obtained from the continuous model are close to the MD simulation results (compare Fig.

IV.4 with Fig. IV.7, and Fig. IV.5 with Fig. IV.8). The hydrodynamical simulation code that we developed would be used by us in further explorations pertaining to the formation of virtual nanojet nozzles, and jet steering (bending) processes.

References

1. L. D. Landau and E. M. Lifshitz, *Fluid Mechanics* (Pergamon, Oxford, 1984).
2. Stanley Middleman, *Modeling axisymmetric flows: dynamics of films, jets and drops*, (Academic Press, San Diego, 1995).
3. John D. Anderson, Jr., *Computational fluid dynamics: the basics with applications* (McGraw-Hill, New York, 1995).
4. Dale A. Anderson, John C. Tannehill, and Richard H. Pletcher, *Computational Fluid Mechanics and Heat Transfer* (Hemisphere Publishing, Washington, 1984).